## TASK I

### Project I.7

# LASER PYROLYSIS PRODUCTION OF NANOSCALE CATALYSTS FOR COAL LIQUEFACTION

**Peter C. Eklund**
**Center for Applied Energy Research**
**University of Kentucky**

## Summary

In this past year, we have systematically investigated the synthesis of 5 - 20 nm dia. Fe-, Mo- and W-based particulate catalysts using a $CO_2$ laser pyrolysis technique. These catalysts include carbides($Fe_3C$, $Fe_7C_3$, $Mo_2C$, $W_2C$), sulfides($Fe_{1-x}S$), nitrides($Fe_3N$, $Fe_4N$, $Mo_2N$, $W_2N$), oxides($Fe_3O_4$, $WO_3$), and metals($\alpha$-Fe, $\gamma$-Fe). Commercial carbonyl compounds including $Fe(CO)_5$, $W(CO)_6$ and $Mo(CO)_6$ have been used as chemical precursors, and $C_2H_4$, $H_2S$, $NH_3$, and $O_2$ as reactant gases. Our success in the synthesis of these catalysts demonstrates that other ceramic catalysts containing V, Hf, etc, whose carbonyl compounds are readily available, can also be prepared using the $CO_2$ laser pyrolysis technique.

We have also extended our $CO_2$ laser pyrolysis to synthesize nanoscale carbon black particles, which might be used as catalysts or as a catalyst support for more expensive metals (e. g., Pt, Mo, etc.) in coal liquefaction. These carbon particles are produced by pyrolyzing benzene($C_6H_6$) with a small amount of $Fe(CO)_5$ as a catalyst. Furthermore, using our laser pyrolysis system, we have produced $FeWO_4$ by pyrolyzing a mixture of $Fe(CO)_5$, $W(CO)_6$, and $O_2$, which demonstrates for the first time that the $CO_2$ laser pyrolysis is also useful to produce stoichiometric, crystalline, and nanoscale *ternary* compounds. This is important since many mixed-valence ternary compounds (e. g. $La_{2-x}Sr_xCuO_4$) have been found to exhibit high catalytic activity.

We have also carried out a study to determine the catalytic benefit of nanoscale Fe-carbide($Fe_7C_3$) and Fe-sulfide($Fe_{1-x}S$) catalysts in the direct liquefaction of subbituminous coal. The results have been compared to those determined for commercial Fe-oxide($Fe_2O_3$) catalysts.

## I. Synthesis and characterization of Fe-, Mo- and W-based nanoscale catalysts

Our upgraded laser pyrolysis system[1] is shown schematically in Fig. 1. Liquid $Fe(CO)_5$ is contained in a glass trap, whereas solid $Mo(CO)_6$ or $W(CO)_6$ is loaded into a sublimation cell developed this year whose temperature can be regulated between 25 and 500 °C. Reactant gases including $C_2H_4$, $NH_3$, $H_2S$, and $O_2$, (or their mixture) either bubble through $Fe(CO)_5$ liquid, or flow through heated $Mo(CO)_6$ and $W(CO)_6$ powder, and then flow vertically out of a stainless

steel nozzle along with the vapors of these precursors, and intersect a horizontal beam from a $CO_2$ laser beam (Laser Photonics Model 150). The reaction is initiated and sustained by the heat generated from resonant absorption of $CO_2$ laser energy by either a reactant gas such as ethylene ($C_2H_4$) or ammonia ($NH_3$), which have strong rotational-vibrational bands that match one of ~100 $CO_2$ laser lines. We display absorption spectra of $C_2H_4$ and $NH_3$, and emission spectra of our $CO_2$ laser in Fig. 2. Important reaction parameters include total chamber pressure, laser power density, reactant gas flow rate, vapor pressure of chemical precursors and reactant gas nozzle diameter. The particles form as a result of the thermal decomposition of metal carbonyl, e. g. $Fe(CO)_5$ -> Fe + $(CO)_5$, and the subsequent reaction of metal ions with the reactant gases. The detailed synthesis process has been described in our paper.

*a. Fe-based catalysts($\alpha$-Fe, $\gamma$-Fe, $Fe_3C$, $Fe_7C_3$, $Fe_3N$, $Fe_4N$, $Fe_3O_4$)*

In Fig. 3, we display XRD data (dots) for nanocrystalline $\alpha$-Fe(3a), $Fe_3C$(3b) and $Fe_7C_3$(3c) generated in our laser pyrolysis system by pyrolyzing a mixture of $Fe(CO)_5$ and $C_2H_4$. The data, corrected for the instrumental zero shift in $2\theta$, were collected using $Cu(K_\alpha)$ radiation using a Phillips 3100 powder diffractometer. The solid lines in the figure were calculated to fit the data using a Lorentzian lineshape for the diffraction peaks and an exponential term $\beta e^{-\gamma x}$ for the background. The values used for the diffraction peak positions and peak areas were taken directly from a standard powder diffraction file. To fit approximately each diffraction scan, a single value for the Lorentzian line width (w, or the full width at half maximum-FWHM) was chosen for $\alpha$-Fe $Fe_3C$, $Fe_7C_3$ and $Fe_3O_4$, respectively. It is clear from the figure that the position and relative intensity of most peaks agree well with the standard powder data, indicating that our identification of the majority phase is correct.

Shown in Fig. 4 are the XRD results for a few batches of particles produced by pyrolyzing a mixture of $Fe(CO)_5$ and $NH_3$. The solid lines are composite curves calculated using sets of Lorentzian functions whose peak positions and intensities were taken from standard powder diffraction data files for each individual phases including $\alpha$-Fe, $\gamma$-Fe, $Fe_3N$, and $Fe_4N$. Note the changes in the XRD pattern as the relative amount of $\alpha$-Fe, $\gamma$-Fe, $Fe_3N$, and $Fe_4N$ varies with $NH_3$ flow rate. This indicates that the relative amount of individual phase is controllable by adjusting reaction conditions, similar to what we have observed in the synthesis of single phase Fe-carbides.

In Fig. 5, we display XRD results for nearly single phase Fe-sulfide ($Fe_{1-x}S$)(5a) and Fe-oxide($Fe_3O_4$)(5b) particles obtained by pyrolyzing mixtures $\{C_2H_4+Fe(CO)_5+H_2S\}$ and $\{C_2H_4+Fe(CO)_5+O_2\}$, respectively. In both synthesis processes, the reaction parameters were adjusted so that $C_2H_4$ does not decompose, yet serves as an absorbing gas subsequently providing heat to the reaction. This is necessary since the other two gases, (i. e., $H_2S$ or $O_2$) do not couple to the $CO_2$ laser energy. The fact that $C_2H_4$ does not decompose for example in the production of $Fe_{1-x}S$ ($W_2N$) is supported by Fig. 5, in which we do not observe any diffraction lines associated with crystalline carbide phases. Furthermore, we have studied $Fe_{1-x}S$ particles using Raman scattering in which we have not found any peaks that may be associated with the presence of pyrolytic carbon in $Fe_{1-x}S$ particles.

*b. Mo and W-based catalysts($Mo_2C$, $Mo_2N$, $W_2C$, and $W_2N$)*

In this section, we describe the synthesis of nanoscale Mo and W carbide and nitride catalysts from solid Mo- and W-carbonyl precursors using our $CO_2$ laser pyrolysis system. Since these carbonyls are solids at room temperature and sublime only in the range 120 ~ 150 °C, we have used our newly installed temperature regulated sublimation cell to generate Mo- or W-carbonyl vapors into the reaction zone. This cell attaches via a copper gasket to the bottom of the stainless steel six-way cross reactor. The concentration of Mo- or W-carbonyl vapors in the reaction zone is thus controlled by regulating the temperatures of the sublimation cell.

We show in Fig. 6 the XRD results of Mo-carbide($Mo_2C$)(Fig. 6a) and W-carbide($W_2C$)(Fig. 6b) particles synthesized by pyrolyzing a vapor phase mixture of $Mo(CO)_6$ and $W(CO)_6$ with $C_2H_4$, respectively. In Fig. 7, we plot XRD data for Mo-nitride($Mo_2N$)(7a) and W-nitride($W_2N$)(7b) particles obtained by pyrolyzing a vapor phase mixture of $Mo(CO)_6$ and $W(CO)_6$ with $NH_3$, respectively. The sharp lines in Fig. 7b are associated with the large $W(CO)_6$ crystalline particles condensed onto the glass trap from unreacted W-carbonyl vapor. In Fig. 7, diffraction line intensity differences between our data and those in the standard powder diffraction data file might indicate stoichiometric differences, or structural defects, in our laser pyrolysis produced particles which may in fact lead to interesting new properties.

Shown in Fig. 8 are the TEM images taken for $Mo_2C$, $W_2C$, $Mo_2N$, and $W_2N$ particles whose XRD spectra have been given in Fig. 7. These particles are spherical and fairly uniform in particle size. The particle size determined from these images is larger than the crystalline size estimated from XRD results using DS equation, indicating that disorder exist within each particle. A heat treatment experiment is underway to see at what temperatures this disorder can be removed.

Raman scattering experiments to look for pyrolytic carbon were carried out on both $W_2C$ and $W_2N$ nano-particles. The dominant structure in $W_2C$ spectra is the broad doublet with peaks centered at 1375 and 1580 $cm^{-1}$. This doublet is the well known result for a disordered pyrolytic carbon. It is clear from the figure that pyrolytic carbon does not exist in the nitride particles. This result is consistent with our previous study on the Fe-carbides and Fe-nitrides, where pyrolytic carbon has only been observed in the case of carbides. This is further supporting our conclusion that surface pyrolytic carbon on our nanoparticles, as observed in the carbides, comes from the thermal decomposition of $C_2H_4$ onto the particle surface, instead of from the CO derived from the carbonyl species.

*c. Nanoscale $WO_3$ and ternary compound $FeWO_4$*

In Fig. 10(a), we show the XRD data for nanoscale $WO_3$ particles obtained by pyrolyzing a mixture of $W(CO)_6$, $O_2$ and $C_2H_4$. Vertical lines in the figure represent standard powder diffraction data file for $WO_3$. Agreement between line positions and intensities of our data and standard file identifies the crystalline phase. However, as synthesized, the particles exhibit a bluish color, indicating an oxygen deficiency. By a simple heat treatment at 300 °C in flowing $O_2$ for 5 hours, the particles were transformed into stoichiometric $WO_3$ which exhibit yellow color at 300 °C and yellow-greenish color at room-temperature.

In Fig. 10(b), we show XRD data of the as synthesized particles produced by using the same sets of reaction parameter values used in the synthesis of $Fe_3O_4$(Fig. 5a), except for the presence of a controlled amount of $W(CO)_6$ vapor in the reaction zone. In a comparison with the XRD spectra for $Fe_3O_4$ given previously in Fig. 5a, we note that majority of additional diffraction lines can be identified as due to the appearance of a $FeWO_4$ phase. Thus, we have demonstrated for the first time that a *crystalline ternary* compound can be obtained using this technique with appropriate sets of reaction parameters.

*d. Nanoscale carbon black particles*

Carbon black particles were produced by pyrolyzing a vapor phase mixture of $Fe(CO)_5$ and $C_6H_6$ introduced into reaction zone by bubbling $C_2H_4$ through a solution of $C_6H_6$:$Fe(CO)_5$ = 50:1(by volume) in the glass container. The $C_2H_4$ flow rate was regulated to be ~100 sccm. Using ~15, 000W/mm$^2$ incident power density in the reaction zone, a bright white flame was observed. If no $Fe(CO)_5$ is present in the stream, almost no soot is produced. From our previous work , if no benzene is present (only $C_2H_4$ and $Fe(CO)_5$), then Fe-carbides are formed. We therefore speculate that $Fe(CO)_5$ in the presence of both $C_2H_4$ and $C_6H_6$ acts as a catalyst, dehydrogenating the benzene and forcing the benzene molecule to fragment in the pyrolysis flame, leading to carbon soot formation. The chemical role of the $C_2H_4$ may not be important, other than to allow heat energy from the laser to be pumped into the reaction. A 0.5g/hour production rate of carbon black was obtained under the conditions described above.

Subsequent to the synthesis, standard elemental analyses were applied to our carbon black samples for Fe, C, N, and H. The results of this analysis yield a composition $C_{10}Fe_{0.01}H_{1.2}N_{0.1}$. It should be noted that the C:H ratio is ~ 8, close to the ideal value ~10 predicted for acetylene black using a polycondensation model , and this value is lower than that obtained for a typical acetylene black, which has C:H ~40. The C:Fe ratio was also measured using electron microprobe analysis (EDX), resulting in C:Fe ~ 700, consistent with the value ~1000 obtained from the elemental analysis.

Shown in Fig. 11 are the high resolution TEM data taken using a JOEL 4000 electron microscope on "as synthesized"(11a, 11b) and heat treated (2800 °C in Ar) (11c, 11d) carbon blacks produced by laser pyrolysis. As shown in Fig. 11a, untreated carbon black particles present, on average, a well developed spherical shape, with an average particle diameter on the order of 20 nm. Typical of acetylene black, significant agglomeration was observed. It is difficult to determine to what extent the particles might be fused, however. Fig. 11b is a magnified image within particle. Although the formation of very primitive carbon planes is observable in some regions of selected particles, most carbon black particles appear to exhibit an image of a highly disordered graphitic carbon (see the discussion of the x-ray results below).

Using the standard $N_2$ BET technique, we determined a value 50 m$^2$/g surface area for the "as-synthesized" carbon black. This value is slightly lower than 70 m$^2$/g reported for a typical acetylene black, and is lower than the theoretical surface total surface area for a 20 nm spherical particles (150 m$^2$/g). Consistent with this observation of a lower surface area, is that no significant cracking of the particle surface or accessible internal pores are apparent in the TEM photos (Fig. 11b) and that agglomeration (with possible fusion) of the particles is also observed.

Furthermore, the carbon black samples subjected to 2800 °C HTT in Ar show clear evidence for graphitization, consistent with lattice fringes from parallel carbon planes and the associated lattice plane spacing(Fig. 11d). As shown in Fig. 11c and 11d, heat treated particles, in many cases, exhibit parallel carbon layers in polygonal shapes about a hollow center. This suggests that crystallization is initiated at the particle surface. Finally, we did not observe any evidence for the presence of Fe or Fe carbides as small particles within the carbon black particle, or, in particular, at the particle core, or as a separate nanoparticle. This is consistent with the small amount of Fe observed in the carbon black (0.5wt %), suggesting that the Fe may be atomically dispersed throughout the soot.

Shown in Fig. 12 are XRD results obtained with a Rigaku powder diffraction unit using Cu $K_\alpha$ radiation. Results for "as synthesized" (Fig. 12a) and low temperature HTT (900 °C in $N_2$) (Fig. 12b) carbon black samples are presented. The low HTT sample was produced with a higher than normal amount of $Fe(CO)_5$. As a result, this sample exhibited x-ray diffraction peaks associated with the existence of nanocrystalline $\alpha$-Fe and $\gamma$-Fe, as indicated. The diffraction peaks for the "as synthesized" sample are similar in width to that of a typical acetylene black. Broad peaks are observed and indexed according to a convention for acetylene blacks based on graphite: in decreasing intensity, they are the 002, 10, and 11 diffraction lines, respectively. The average lattice constant along the c-axis, as determined from the 002 peak position, is found to be 3.65 Å, somewhat larger than normally observed (<3.5 Å) for acetylene black. A significant shift of 002 peak is observed after a 900 °C HTT in $N_2$ for 24 hrs(Fig. 12b), where again from the 002 peak, the lattice constant has decreased to 3.48 Å, closer to that of a typical acetylene black (3.43 Å).

## II. Studies of relative activity of nanoscale iron oxide, iron carbide, and iron sulfide catalyst precursors for the liquefaction of a subbituminous coal

*a. Experiment*

Three nanoscale iron-based catalysts were utilized in this study.Iron carbide and iron sulfide were obtained using our laser pyrolysis system. The XRD spectrum of the particles confirmed the production of $Fe_{(1-x)}S$. Table 1 shows the reaction parameters used for the production of the pyrrhotite particles. The iron sulfide particles were paramagnetic, therefore the ferromagnet was removed and the particles were separated from the gas stream by the teflon filter. The as-formed particles were less pyrophoric than the iron carbide phase but still required passivation prior to removing from the trap. The third catalyst used in this study, a superfine iron oxide (SFIO), was provided by Mach I Inc. and was reported to be a 30 Å diameter $\alpha$-$Fe_2O_3$ particle. The properties of the three catalyst used in this study, as determined by XRD and nitrogen BET adsorption measurements, are presented in Table 2.

Liquefaction experiments were carried out in 50 ml horizontal microautoclave reactors, a configuration that reduces mass transfer limitations. The reactors were agitated at 400 cycles/minute in a heated fluidized sand bath. This allowed the rapid (<2 minutes) attainment of reaction temperature and thereby minimized errors associated with long heat-up times. The microautoclaves were loaded with 3 g of a subbituminous Black Thunder coal and 5 g of tetralin, used as a hydrogen donor solvent. An analysis of the coal is shown in Table 3. Catalyst loadings

of 0.7 and 1.4 wt % Fe on as-received coal were used, corresponding to 1 and 2 wt % Fe on maf coal respectively, and dimethyldisulfide (DMDS) was added as a sulfiding agent in these runs. The reactors were sealed purged and pressurized to 1000 psig (cold) with hydrogen.

A set of blank liquefaction experiments were carried out in the absence of coal to determine the effect of sulfur on the iron carbide particles under liquefaction conditions. A microautoclave reactor was loaded with 0.2 g of $Fe_7C_3$, 5g tetralin, and DMDS at twice the stoichiometric loading needed to form $FeS_2$, and reacted at 385 °C for 30 minutes. The residue from the run was collected and analyzed by XRD.

Two sets of conditions were used in this study. A low severity condition of 385°C for 15 minutes and a high severity condition of 415°C for 60 minutes. After reaction, the microautoclaves were quenched in a cool fluidized sand bath. A sample of the gas phase of the reactor was removed for analysis by gas chromatography. The contents of the cooled reactors were removed using tetrahydrofuran (THF) and were analyzed by solubility class. All conversions were determined and reported on a maf coal basis. Total conversion was defined by THF solubility. The THF insoluble material was defined as insoluble organic matter (IOM) while the THF soluble, pentane insoluble fraction was defined as preasphaltenes + asphaltenes (PA&A). The oil yield, contained in the pentane soluble fraction, was determined by difference. All liquefaction experiments were done in duplicate to ensure reproducability.

The amount of solvent dehydrogenation was calculated from the naphthalene/tetralin ratio determined by GC analysis of the pentane soluble fraction. The H/C ratio of the PA&A fraction was determined by elemental analysis. The phase of the catalyst, as well as the average crystallite diameter, was determined from XRD spectrum. Surface area was measured using a nitrogen BET adsorption method.

*b. Results and Discussion*

Due to the small size of the SFIO particles, which severely limited the use of traditional characterization techniques such as XRD, there is some speculation on the actual phase. One recent study, using Mössbauer and XAFS spectroscopies, reported that the major phase is ferrihydrite [2]. Another study has identified the major phase as $\gamma$-$Fe_2O_3$ based on energy-dispersive X-ray and microdiffraction [3]. This material is reported to be extremely sensitive to moisture and to tend to form large (~150 Å) particles of $\alpha$-$Fe_2O_3$ [4]. For the purposes of this study the SFIO will be considered to be $Fe_2O_3$ for the calculations of conversion and iron loadings.

The iron carbide formed by the laser pyrolysis technique was passivated prior to exposure to air. XPS studies of the passivated material indicated that some of the surface of the particles becomes oxidized, while XRD shows the bulk remained in the carbide phase. Similarly, the iron sulfide particles also were passivated though they were less pyrophoric than the carbide particles.

The results of the nitrogen BET adsorption measurements showed that there was very little porosity associated with any of the materials used in this study. Therefore, unlike supported catalysts, in which much of the surface area is associated with small micropores, the bulk of the active sites were on the external surface area and therefore readily accessible to the coal. The

results of the catalyst precursor characterization studies, shown in Table 2, indicate that the SFIO contained the smallest particles (3 nm diameter) and consequently the highest surface area (195 $m^2/g$). The XRD spectra indicate that the diameter of the iron sulfide and iron carbide were very similar (14 and 17 nm respectively), although their surface areas differed significantly (42 and 95 $m^2/g$ respectively), reasons for which are not clear.

While it has been shown that iron oxide, in the presence of sufficient sulfur, will transform to pyrrhotite under liquefaction conditions [5], the behavior of the iron carbide was not known. The results of the blank runs showed that the transformation to pyrrhotite was complete within 30 minutes at 385°C, indicating that the iron carbide does not possess the stability reported to exist for molybdenum and tungsten carbides [6-8]. While the pyrrhotite does not undergo a phase change it is possible that the stoichiometry will change as a function of the sulfur concentration in the system[9,5].

The results of the liquefaction experiments, summarized in Table 4, indicate that, at the high severity conditions and a catalyst precursor loading of 0.7 wt % Fe on as-received coal, all three precursors yielded nearly identical catalytic effects resulting in an increase in the total conversion from 81 wt% for the thermal runs to 87 wt % for the catalytic runs. The enhanced total conversion, shown in Figure 13, appears to be due solely to the increase in oil yield while the PA&A and gas yields show no significant deviation from the thermal baseline. Increasing the iron concentration to 1.4 wt % showed some further increase in total conversion for each precursor with $Fe_7C_3$ at 89 wt%, $Fe_{(1-x)}S$ at 87 wt%, and SFIO at 88 wt %. Again, the increase is due mainly to an increase in oil yield. As shown in Figure 14, in the case of the $Fe_{(1-x)}S$ and the SFIO precursors, slight decreases in the PA&A yield were also observed.

Liquefaction experiments were conducted at the low severity conditions to minimize thermal effects and to maximize the effect of the catalyst precursors. Further, since it had been shown that both the carbide and the oxide precursors transform to a sulfide phase under liquefaction conditions, the longer reaction time used in the high severity experiments may have also obscured the distinctions between the catalyst precursors.

The results, shown in Figure 15, indicate that at the low severity conditions there are only minor differences in catalytic activity for an iron loading of 0.7 wt %. The $Fe_{(1-x)}S$ showed the highest activity with a total conversion, 52.6 wt %, followed by SFIO at 52.2 wt %, $Fe_7C_3$ at 50.3 wt %, compared to a thermal conversion of 46.2 wt %. The changes were mostly apparent as increases in PA&A with little change in the oil or gas yields. This indicates that there is little difference in the effect of the three iron based catalyst precursors on the conversions regardless of the form of the added precursor.

The amount of hydrogen consumption showed a strong dependence on the phase of the catalyst precursor, particularly at high severity. Under low severity conditions, at a loading of 0.7 wt % Fe, the effect of precursor phase on the amount of total hydrogen uptake is minimal, each showing a similar increase over the thermal baseline. The increase of severity to 415 °C for 60 minutes shows a marked increase in the total hydrogen consumption, as shown in Figure 16, with the $Fe_{(1-x)}S$ and $Fe_7C_3$ precursors showing similar behavior. The SFIO, at these conditions, caused significantly greater total hydrogen uptake. The hydrogen consumed from the gas phase follows

the trend thermal < $Fe_7C_3$ < $Fe_{(1-x)}S$ << SFIO while the solvent dehydrogenation followed the opposite, though less distinct, trend. The higher gaseous hydrogen consumption and lower solvent dehydrogenation indicates a higher hydrogenation activity for the SFIO. This is particularly interesting since the liquefaction yields showed the effect of these catalysts to be nearly identical. This would appear to indicate that bond cleavage, rather than the availability of labile hydrogen, was the main factor in limiting the total conversion. Increasing the iron concentration to 1.4 wt % has a significant impact on the total hydrogen consumption for the $Fe_7C_3$ and the $Fe_{(1-x)}S$ bringing them closer to the uptake of the SFIO, which still causes significantly less solvent dehydrogenation, as shown in Figure 16.

The H/C ratio for the PA&A fraction showed that the additional uptake of hydrogen for the SFIO was, in part, incorporated into these products. The increase in H/C ratio with increasing SFIO concentration followed a trend similar to the hydrogen consumption, as shown in Figures 17 and 18, respectively. A similar propensity was also observed for $Fe_7C_3$. This may be indicative of an increase in conversion from preasphaltenes to asphaltenes which was not discernable by the separation methods used in this study. However, the $Fe_{(1-x)}S$ at a catalyst loading of 1.4 wt % Fe showed a decrease in H/C ratio to near that of the thermal reaction. This may indicate that, for the $Fe_{(1-x)}S$, the increased hydrogen consumed was primarily utilized in improving the quality, though not the quantity, of the oil fraction. Confidence in this data was high due to the fact that the runs were made in duplicate with a standard deviation of less than ±3.5%.

The final phase of the iron based catalysts in a coal liquefaction process is pyrrhotite, provided that sufficient sulfur is present to allow that transformation. As previously noted, the conversion of the carbide phase occurs within 30 minutes at 385 °C. The conversion of the catalyst precursor may occur by reduction of the surface oxide or carbide followed by sulfidation of the reduced iron sites [10]. The sulfur then diffuses into the particle as the internal oxygen or carbon diffuses to the surface where it reacts with the hydrogen. Since the activity of the particles is associated with active sites located on the surface, the various precursors probably exhibit similar catalytic effects very early in the reaction. This would explain the fact that the conversions obtained using pyrrhotite as the catalyst precursor were no more favorable than those obtained from the other precursors. Further, the activity of the SFIO for solvent hydrogenation is significantly higher than the $Fe_{(1-x)}S$ which was in turn slightly higher than $Fe_7C_3$. Particularly for the high severity conditions, the difference in hydrogenation activity is probably related to the surface area, rather than the phase, of the precursor.

The study by Stohl [11] which reported that the surface area of the precursor had no correlation with the conversion agrees well with the findings of this study. However, while the surface area, or particle diameter, had no effect on the total conversion, the effect on hydrogenation was profound. The relation between solvent dehydrogenation and surface area, as determined from nitrogen BET measurements, shown in Figure 19, indicates that, particularly at higher severity, there is a distinct negative trend. Similarly, Figure 20 indicates an inverse correlation between the total hydrogen consumption and the particle diameter. This appears to indicate that the hydrogenation activity related to the catalyst precursors is much more closely related to the particle diameter, or amount of surface area available for reaction, than to the phase of the catalyst precursor.

The specific surface area, which is defined as the surface area per 100g maf coal, may be a measure of the catalytic sites available to the coal for reaction. Using this number, a plot for all experiments conducted at high severity may be constructed, as shown in Figure 21. The total hydrogen consumption increases rapidly at low specific surface areas followed by a plateau at higher specific surface areas. This may indicate a saturation condition above which increasing catalyst concentration will produce minimal benefit. This would explain the greater effect of increasing the catalyst loading for $Fe_{(1-x)}S$ and $Fe_7C_3$ compared to SFIO as shown in Figure 16. The greater specific surface area of the SFIO results in more rapid attainment of the saturation at lower concentrations, yielding minimal benefit for additional catalyst loading.

Finally, we summarize that the three catalysts tested in this study, $Fe_7C_3$, $Fe_{(1-x)}S$, and SFIO, demonstrate very similar activity with respect to the conversion of a subbituminous coal. At lower severity the primary effect of 0.7wt % Fe catalyst loading was represented by a slight (4-6 wt %) increase in the total conversion. This was mostly associated with an increase in the PA&A yield. At higher severity the same catalyst loading resulted in a 6-7 wt % increase in total conversion, almost exclusively associated with an increase in the oil yield. This indicates an improvement in catalyst selectivity, as well as activity for conversion. Doubling the catalyst concentration to 1.4 wt % Fe resulted in only minor changes to the conversion, but effected some increase in the selectivity to oils, particularly for the SFIO and $Fe_{(1-x)}S$ precursors.

The effects of the different catalyst precursors on hydrogen consumption from the gas phase and the extent of solvent dehydrogenation were more pronounced. For the high severity conditions, at a catalyst loading of 0.7 wt % Fe, the total amount of hydrogen consumed followed the trend thermal<$Fe_7C_3$<$Fe_{(1-x)}S$<<SFIO. The amount of hydrogen consumed from the gas phase followed a similar trend while the amount of solvent dehydrogenation followed the opposite, though much less distinct, trend. The increase in hydrogenation activity correlates well with precursor particle diameter. This indicates that the difference in activity may not be a function of the phase of the catalyst precursor, but rather of the particle size, or available surface area.

The increase of the catalyst concentration to 1.4 wt % further increased the hydrogen consumption but narrowed the gap between the SFIO and the other two precursors. This may be explained as nearing a saturation of the specific surface area of catalyst available for reaction. As this plateau is approached, increasing the catalyst loading results in minimal additional benefit.

## III. References


1. Haggerty, J. S., "Sinterable Powders form Laser-Driven Reactions", in Laser Induced Chemical Processes, J. I. Steinfeld, ed., Plenum Press, New York, 1981
2. Zhao, J.; Huggins, F. E.; Feng, Z.; Lu, F.; Shah, N.; Huffman, G. P., Submitted to *J.Catalysis*.
3. Srinivasan, R.; Keogh, R. A.; Davis, B. H., ACS Div. of Fuel Chem. Preprints, *38* (1) 203-10 (1993).
4. Feng, Z.; Zhao, J.; Huggins, F. E.; Huffman, G. P., Submitted to *J.Catalysis*.
5. Wang, L.; Cui, Z.; Lui, S., *Fuel*, **71**, 755-9, 1992.
6. Oyama, S. T.; Schlatter, J. C.; Metcalfe, J. E.; Lambert, J. M., *I&EC Research, 27,* 1639-48 (1988).
7. Schlatter, J. C.; Oyama, S. T.; Metcalfe, J. E.; Lambert, J. M., *I&EC Research, 27,* 1648-53(1988).
8. Sajkowski, D. J.; Oyama, S. T., ACS Div. of Fuel Chem. Preprints, *35* (2) 233-36 (1990).
9. Montano, P. A.; Vaishnava, P. P.; King, J. A.; Eisentrout, E. N., *Fuel*, **60**, 712-6, 1981.
10. Kamiya, Y.; Nobusawa, T.; Futamura, S., *Fuel Proc. Tech.*, **18**, 1-10, 1988.
11. Stohl, F. V., *Fuel*, **62**, 122-6, 1983.

# Presentations and Publications Associated with the CFFLS Project (May, 1992 - May, 1993)

*"Structural and Surface Studies of Nanocrystalline Iron Carbides"*, presentation, A. R.Sethuraman, A.M. Rubel, Xiang-Xin Bi, P. C. Eklund, G. T. Hager, F. J. Derbyshire and J. M. Stencel, Materials Research Society Meeting, San Francisco, CA, April 27 - May 1, 1992.

*"In-Situ High Temperature X-Ray Diffraction Studies of Nanocrystalline Iron Carbides"*, presentation, A. R. Sethuraman, Xiang-Xin Bi, P. C. Eklund, J. M. Stencel, O. B. Cavin and C. R. Hubbard, Materials Research Society Meeting, San Francisco, CA, April 27 - May 1, 1992.

*"Nanoscale Fe-based Catalysts for Coal Liquefaction"*, presentation, P. C. Eklund, Xiang-Xin Bi, F. J. Derbyshire, 6th Annual Technical Meeting of the Consortium for Fossil Fuel Liquefaction Science, Wheeling, WV, July 28 - 31, 1992.

*"Synthesis and Physical Properties of Nanosize α-Fe, $Fe_3C$, $Fe_7C_3$ and $Fe_xS_y$ Particles"*, presentation, Xiang-Xin Bi, S. Sinha and P. C. Eklund, Materials Research Society Meeting, Boston, Mass, Dec. 2 - 6, 1992.

*"Nanoscale Fe-Based Catalysts from Laser Pyrolysis"*, presentation, P. C. Eklund, Xiang-Xin Bi, and F. J. Derbyshire, invited talk, Amer. Chem. Soc. meeting, Wash. D. C., 1992.

*"Synthesis and Characterization of Laser Pyrolysis Produced Nanoscale Particles"*, *poster*, Xiang-Xin Bi, P. C. Eklund, T. Hager and F. J. Derbyshire, Gordon Research Conference (Hydrogen Carbon Science), Oahu, Hawaii, November 8 - 13, 1992.

*"Carbide Catalysts: Laser Pyrolysis Synthesis and Catalytic Activity"*, presentation, J. M. Stencel, P. C. Eklund, Xiang-Xin Bi, B. H. Davis, G. T. Hager and F. J. Derbyshire, ICC Conference, Budapest, Hungary, July 19 - 24, 1992.

*"Iron Ultrafine Particle Catalysts Formed by Laser Pyrolysis: Synthesis, Characterization and Coal Liquefaction Activity"*, J. M. Stencel, P. C. Eklund, Xiang-Xin Bi, and F. J. Derbyshire, Catalysis Today, 15, 285(1992).

*"Synthesis of Nanocrystalline Fe-based Particles by $CO_2$ Laser Pyrolysis"*, X.-X. Bi and P. C. Eklund, Proc. of Materials Research Society Meeting (Boston, Mass., Dec. 2 - 6, 1992).

*"Laser Pyrolysis Production of Nanoscale Carbon Black"*, presentation, Xiang-Xin Bi, Wen-Tse Lee and P. C. Eklund, ACS meeting (Fuel Chemistry Division), Denver, Colorado, March 28 - April 2, 1993.

*"Influcence of Nanosize F1-xS Particles on Coal liquefaction"*, presentation, G. T. Hager, Xiang-Xin Bi, P. C. Eklund and F. J. Derbyshire, sumbitted to ACS(Fuel Chemistry Division), Denver, Colorado, March 28 - April 2, 1993.

*"Laser Pyrolysis Production of Nanoscale Carbon Black"*, X.-X. Bi, Wen-Tse Lee and P. C. Eklund, preprint of ACS meeting(Fuel Chemistry Division)(Denver, Colorado, March 28 - April 2, 1993).

*"Nanocrystalline α-Fe, $Fe_3C$ and $Fe_7C_3$ produced by $CO_2$ laser pyrolysis"*, X.-X. Bi, B. Ganguly, G. Huffman, E. Huggines, M. Endo, and P. C. Eklund, J. of Material Research, in press, 1993.

*"Relative Activity of Nanoscale Iron Oxide, Iron Carbide, and Iron Sulfide Catalyst Precursors for the Liquefaction of a Subbituminous Coal"*, G. T. Hager, Xiang-Xin Bi, P. C. Eklund, E. N. Givens, and F. J. Derbyshire, sumbitted to Energy&Fuel, 1993.

Figure Captions:

Fig. 1 $CO_2$ laser pyrolysis system for the synthesis of nanoscale particles.

Fig. 2 Absorption lines of $NH_3$(a) and $C_2H_4$(b), and emission lines of our CW $CO_2$ laser(c).

Fig. 3 XRD data of nanoscale α-Fe (a) and Fe-carbide($Fe_3C$ (b), $Fe_7C_3$ (c)) particles obtained by pyrolyzing $Fe(CO)_5$ with $C_2H_4$. Solid lines are calculated using a set of Lorentzian lines whose peak positions and intensities are obtained from standard powder diffraction data files.

Fig. 4 Examples of X-ray diffraction data on preliminary Fe-N samples. Laser pyrolysis of $Fe(CO)_5$+$NH_3$ was used to produce nanoscale particles. The relative amount of $Fe_3N$ and $Fe_4N$ can be controlled by adjusting the reaction conditions. Solid lines are calculated as in Fig. 3 from standard powder diffraction data file using a variable which controls the relative amount of α-Fe, γ-Fe, $Fe_3N$ and $Fe_4N$. Relative percentage of each phase is given in the figure.

Fig. 5 XRD data of nanoscale Fe-oxide($Fe_3O_4$(a)) and Fe-sulfide($Fe_{1-x}S$(b)) particles obtained by pyrolyzing $Fe(CO)_5$ with $O_2$ and $H_2S$, respectively. Solid lines are calculated using a set of Lorentzian lines whose peak positions and intensities are obtained from standard powder diffraction data files.

Fig. 6 XRD data of nanoscale Mo-carbide($Mo_2C$(a)) and W-carbide($W_2C$(b)) particles obtained by pyrolyzing $Mo(CO)_6$ and $W(CO)_6$ with $C_2H_4$, respectively. Solid lines are calculated using a set of Lorentzian lines whose peak positions and intensities are obtained from standard powder diffraction data files.

Fig. 7 XRD data of nanoscale Mo-nitride($Mo_2N$(a)) and W-nitride($W_2N$(b)) particles obtained by pyrolyzing $Mo(CO)_6$ and $W(CO)_6$ with $NH_3$, respectively. Solid lines are calculated using a set of Lorentzian lines whose peak positions and intensities are obtained from standard powder diffraction data files.

Fig. 8(a) TEM images of nanoscale Mo-carbide($Mo_2C$) particles.

Fig. 8(b) TEM images of nanoscale W-carbide($W_2C$) particles.

Fig. 8(c) TEM images of nanoscale Mo-nitride($Mo_2N$) particles.

Fig. 8(d) TEM images of nanoscale W-nitride($W_2N$) particles.

Fig. 9 Raman spectra(λ=488 nm, Ar, T=300 K) of $W_2N$ and $W_2C$ particles. The peaks that are indicated by the arrows are associated with pyrolytic carbon coating on the particle surface.

Fig. 10 (a) XRD data of W-oxide($WO_3$) nanoscale particles by pyrolyzing $W(CO)_6$ with $O_2$. (b) A mixture of nanoscale phases containing the ternary phase $FeWO_4$ as obtained by adding $W(CO)_6$ to the reaction zone. Vertical lines are from standard powder diffraction data files.

Fig. 11(a,b) High resolution TEM images for as synthesized carbon black particles from our laser pyrolysis system.

Fig. 11(c,d) High resolution TEM images for heat treated carbon black particles (2800 °C, in Ar)

Fig. 12 XRD data for as synthesized carbon black particles (a) and heat treated particles (b) (900 °C, in $N_2$). Vertical lines represent standard powder diffraction data file for α-Fe and γ-Fe.

**Table 1. Typical Reaction Parameters used in Laser Pyrolysis**

| | α-Fe | $Fe_3C$ | $Fe_7C_3$ | $Fe_{(1-x)}S$ |
|---|---|---|---|---|
| Laser Intensity, W | 30 | 50 | 54 | 70 |
| Beam Width, mm | 1 | 1 | 0.2 | 1 |
| Nozzle Diameter, mm | 1.7 | 0.8 | 0.8 | 1.8 |
| Chamber Pressure, torr | 100 | 300 | 500 | 300 |
| Ethylene Flowrate, sccm | 9 | 9 | 25 | 25 |
| $H_2S$ Flowrate, sccm | 0 | 0 | 0 | 5 |

**Table 2. Catalyst Characterization Data**

| | Phase (XRD) | Diameter (nm) (XRD) | Surface Area ($m^2/g$) |
|---|---|---|---|
| SFIO | *see text* | 3 | 195 |
| Iron Sulfide | $Fe_{(1-x)}S$ | 14 | 42 |
| Iron Carbide | $Fe_7C_3$ | 17 | 92 |

**Table 3. Analysis of Black Thunder Coal**

| Proximate | wt% | Ultimate | wt% dry | Sulfur | wt % maf |
|---|---|---|---|---|---|
| Moisture | 22.4 | Carbon | 72.15 | Total Sulfur | 0.39 |
| Ash | 5.46 | Hydrogen | 4.34 | Pyritic Sulfur | 0.07 |
| Volatile Matter | 34.4 | Nitrogen | 1.23 | Sulfate | 0.09 |
| Fixed Carbon | 39.8 | Sulfur | 0.53 | Organic Sulfur | 0.30 |
| | | Oxygen (diff) | 15.93 | | |
| | | Ash | 5.81 | | |

## Table 4. Summary of Coal Liquefaction Conversion Data

| Catalyst | Loading | Severity[1] | % Total Conversion | % PA & A | % Oils | %Gas |
|---|---|---|---|---|---|---|
| None | | Low | 46.2 | 32.6 | 9.7 | 4.0 |
| $Fe_{(1-x)}S$ | 0.7 | Low | 52.6 | 38.3 | 10.4 | 3.9 |
| $Fe_7C_3$ | 0.7 | Low | 50.3 | 35.7 | 10.4 | 4.2 |
| SFIO | 0.7 | Low | 52.2 | 38.7 | 9.4 | 4.1 |
| None | | High | 80.6 | 44.6 | 29.3 | 6.8 |
| $Fe_{(1-x)}S$ | 0.7 | High | 87.1 | 45.3 | 35.0 | 6.8 |
| $Fe_7C_3$ | 0.7 | High | 87.6 | 44.4 | 36.3 | 7.0 |
| SFIO | 0.7 | High | 87.0 | 45.2 | 34.6 | 7.2 |
| $Fe_{(1-x)}S$ | 1.4 | High | 87.0 | 41.7 | 38.2 | 7.0 |
| $Fe_7C_3$ | 1.4 | High | 89.4 | 45.0 | 37.5 | 6.9 |
| SFIO | 1.4 | High | 88.1 | 42.5 | 38.3 | 7.3 |

[1] Low severity = 385°C for 15 minutes
High severity = 415°C for 60 minutes

Fig. 1 $CO_2$ laser pyrolysis system for the synthesis of nanoscale particles.

Fig. 2 Absorption lines of $NH_3$(a) and $C_2H_4$(b), and emission lines of our CW $CO_2$ laser(c).

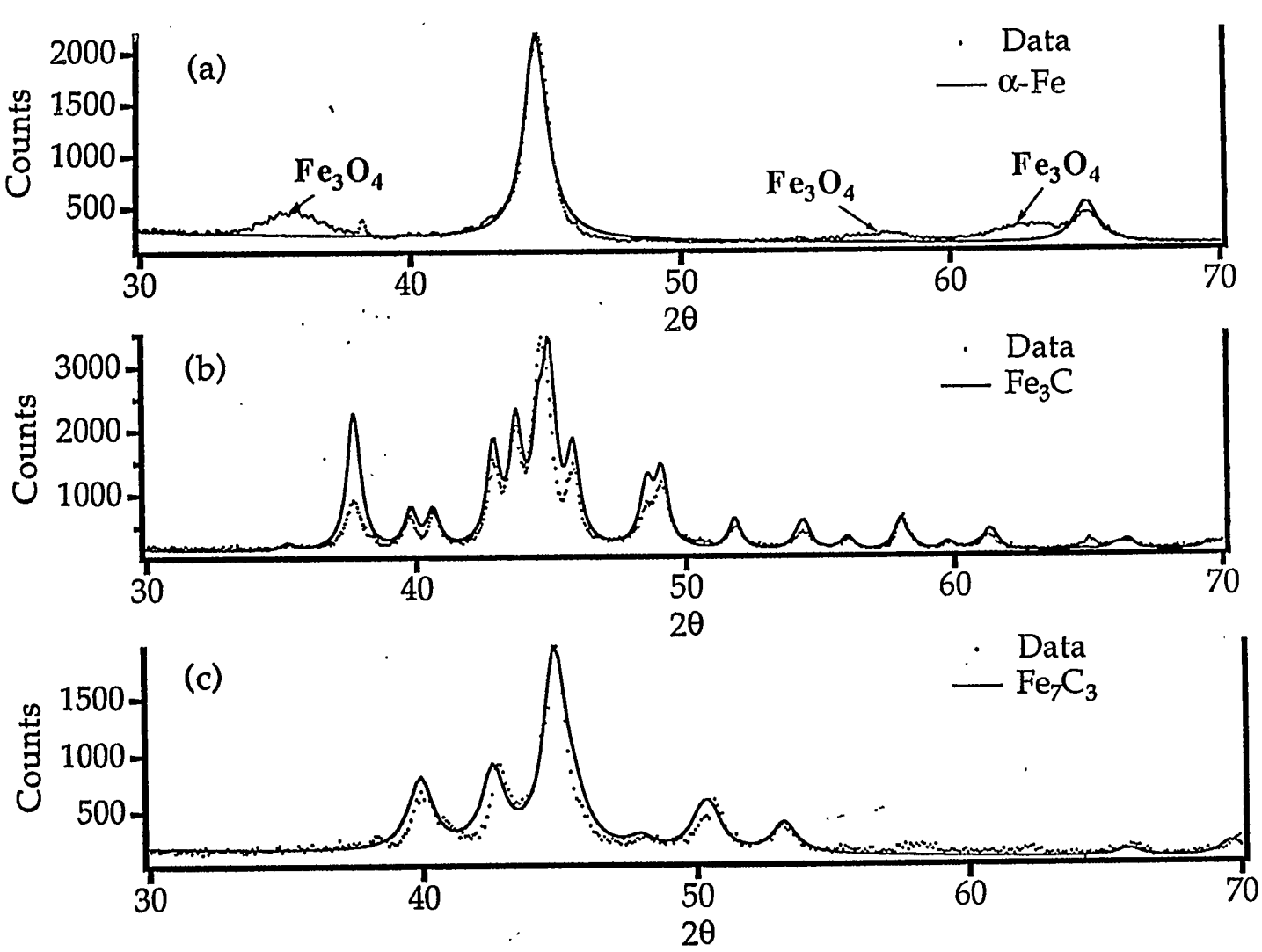


Fig. 3 XRD data of nanoscale α-Fe (a) and Fe-carbide($Fe_3C$ (b), $Fe_7C_3$ (c)) particles obtained by pyrolyzing $Fe(CO)_5$ with $C_2H_4$. Solid lines are calculated using a set of Lorentzian lines whose peak positions and intensities are obtained from standard powder diffraction data files.

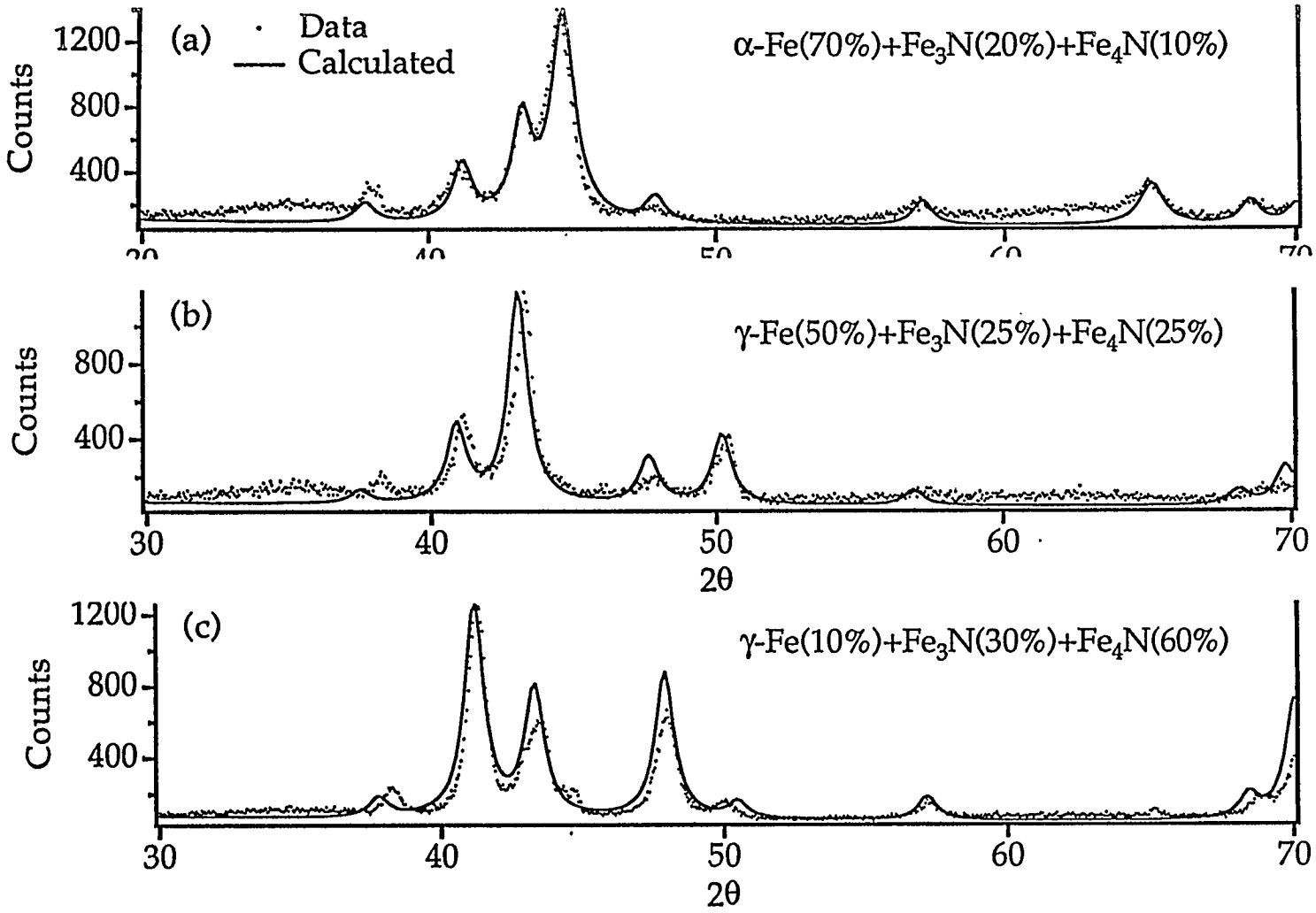


Fig. 4 Examples of X-ray diffraction data on preliminary Fe-N samples. Laser pyrolysis of $Fe(CO)_5$+$NH_3$ was used to produce nanoscale particles. The relative amount of $Fe_3N$ and $Fe_4N$ can be controlled by adjusting the reaction conditions. Solid lines are calculated as in Fig. 3 from standard powder diffraction data file using a variable which controls the relative amount of α-Fe, γ-Fe, $Fe_3N$ and $Fe_4N$. Relative percentage of each phase is given in the figure.

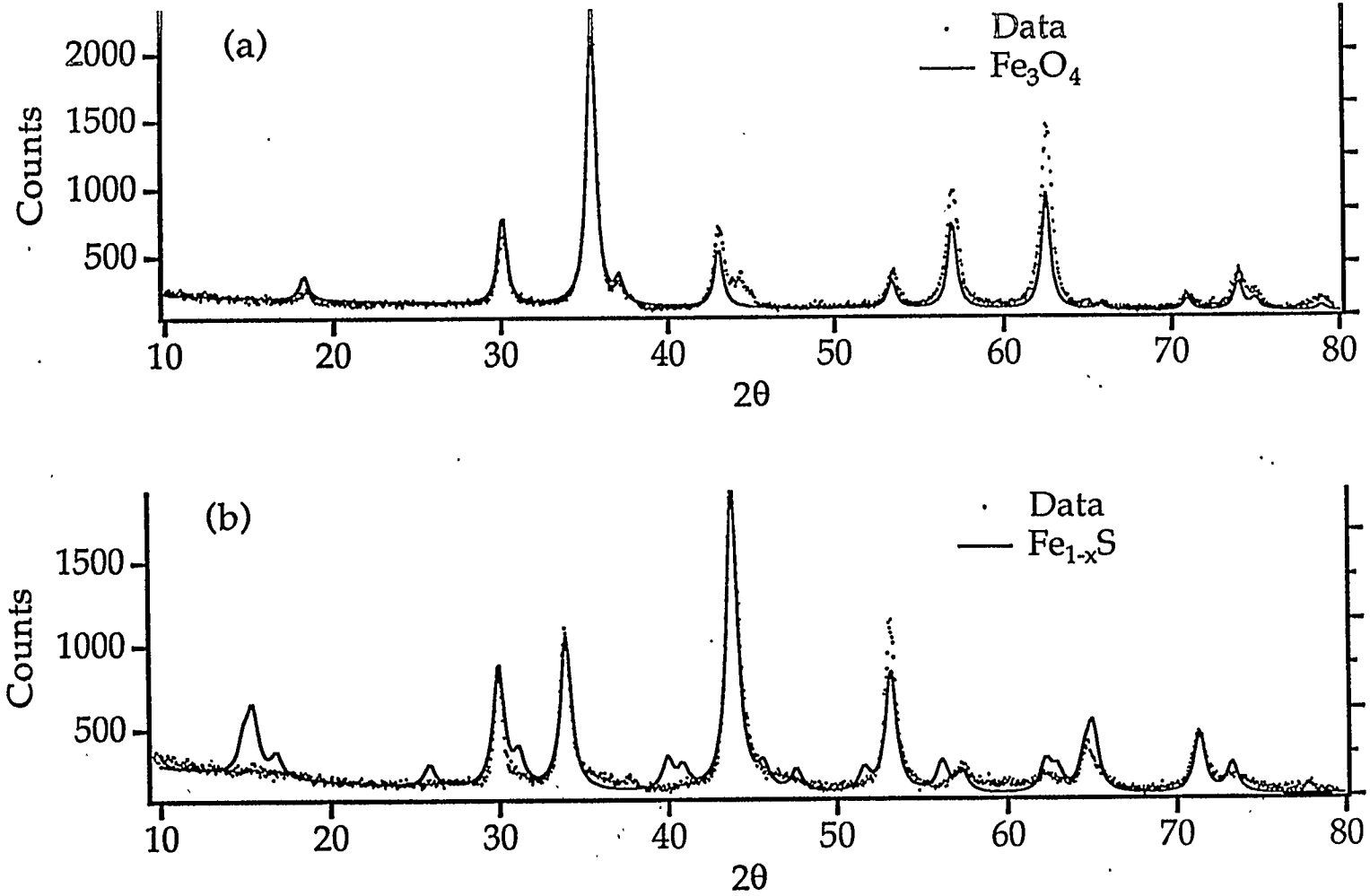


Fig. 5 XRD data of nanoscale Fe-oxide($Fe_3O_4$(a)) and Fe-sulfide($Fe_{1-x}S$(b)) particles obtained by pyrolyzing $Fe(CO)_5$ with $O_2$ and $H_2S$, respectively. Solid lines are calculated using a set of Lorentzian lines whose peak positions and intensities are obtained from standard powder diffraction data files.

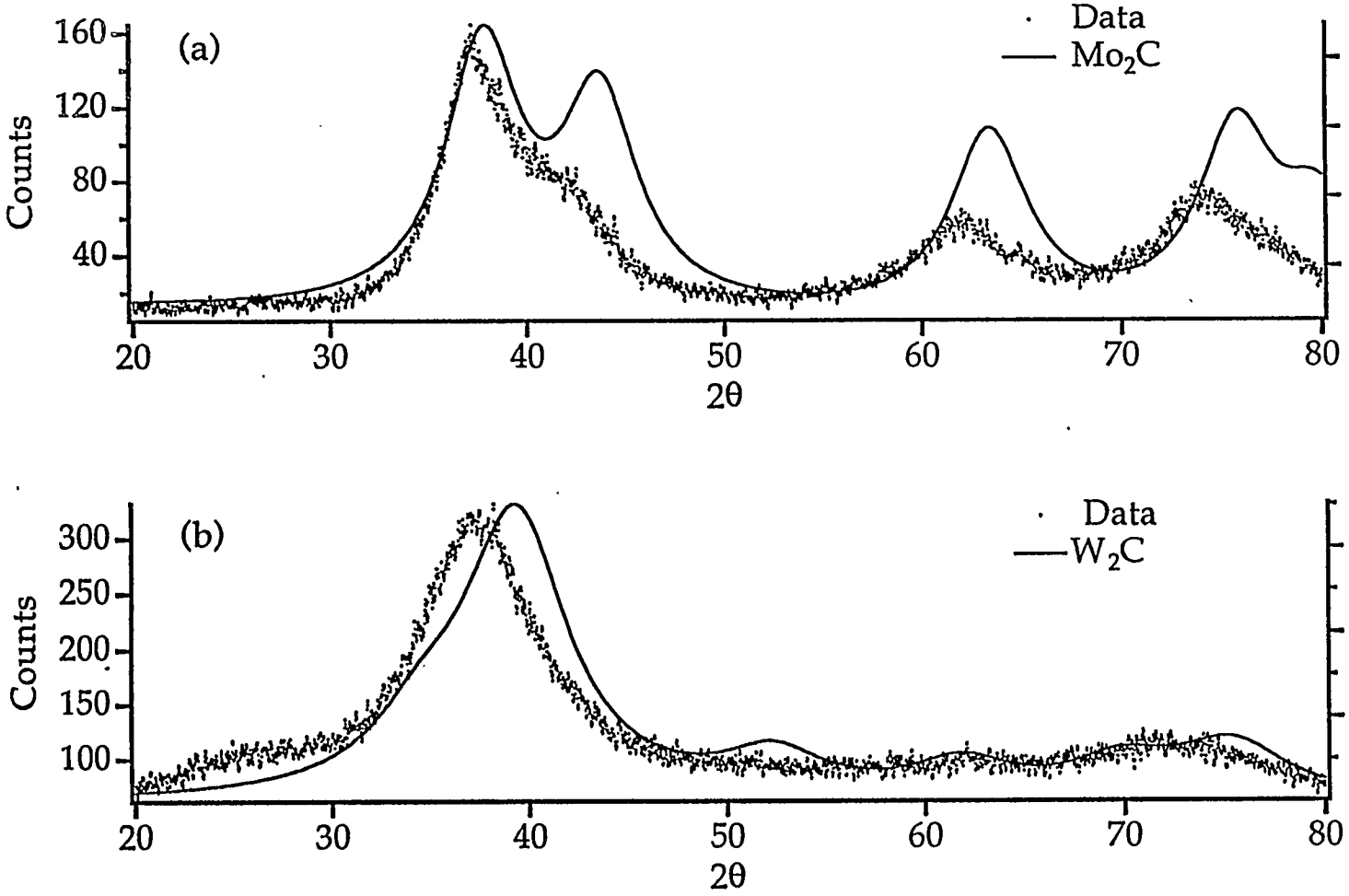


Fig. 6 XRD data of nanoscale Mo-carbide($Mo_2C$(a)) and W-carbide($W_2C$(b)) particles obtained by pyrolyzing $Mo(CO)_6$ and $W(CO)_6$ with $C_2H_4$, respectively. Solid lines are calculated using a set of Lorentzian lines whose peak positions and intensities are obtained from standard powder diffraction data files.

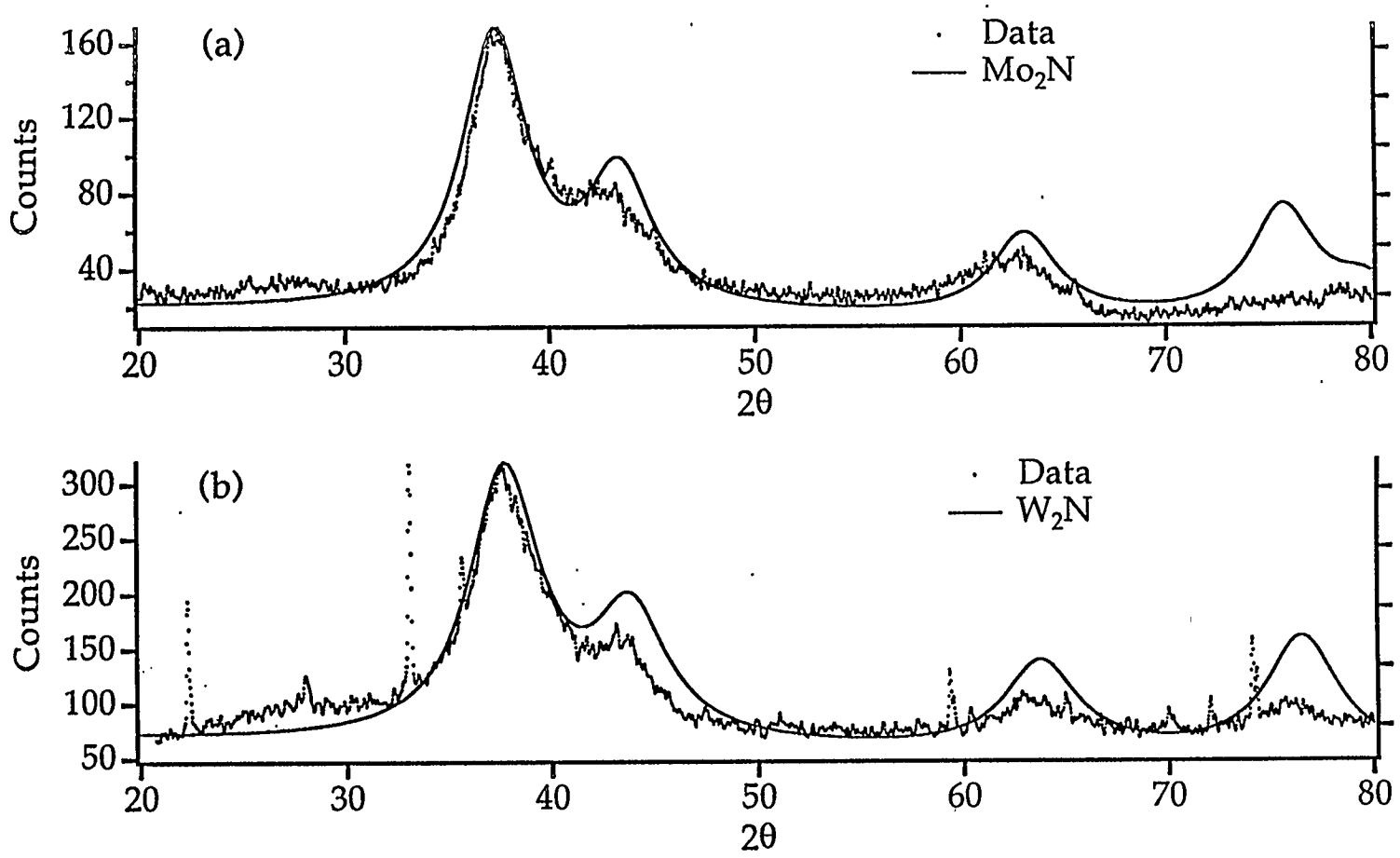


Fig. 7 XRD data of nanoscale Mo-nitride($Mo_2N$(a)) and W-nitride($W_2N$(b)) particles obtained by pyrolyzing $Mo(CO)_6$ and $W(CO)_6$ with $NH_3$, respectively. Solid lines are calculated using a set of Lorentzian lines whose peak positions and intensities are obtained from standard powder diffraction data files.

Fig. 8(a) TEM images of nanoscale Mo-carbide($Mo_2C$) particles.

Fig. 8(b) TEM images of nanoscale W-carbide($W_2C$) particles.

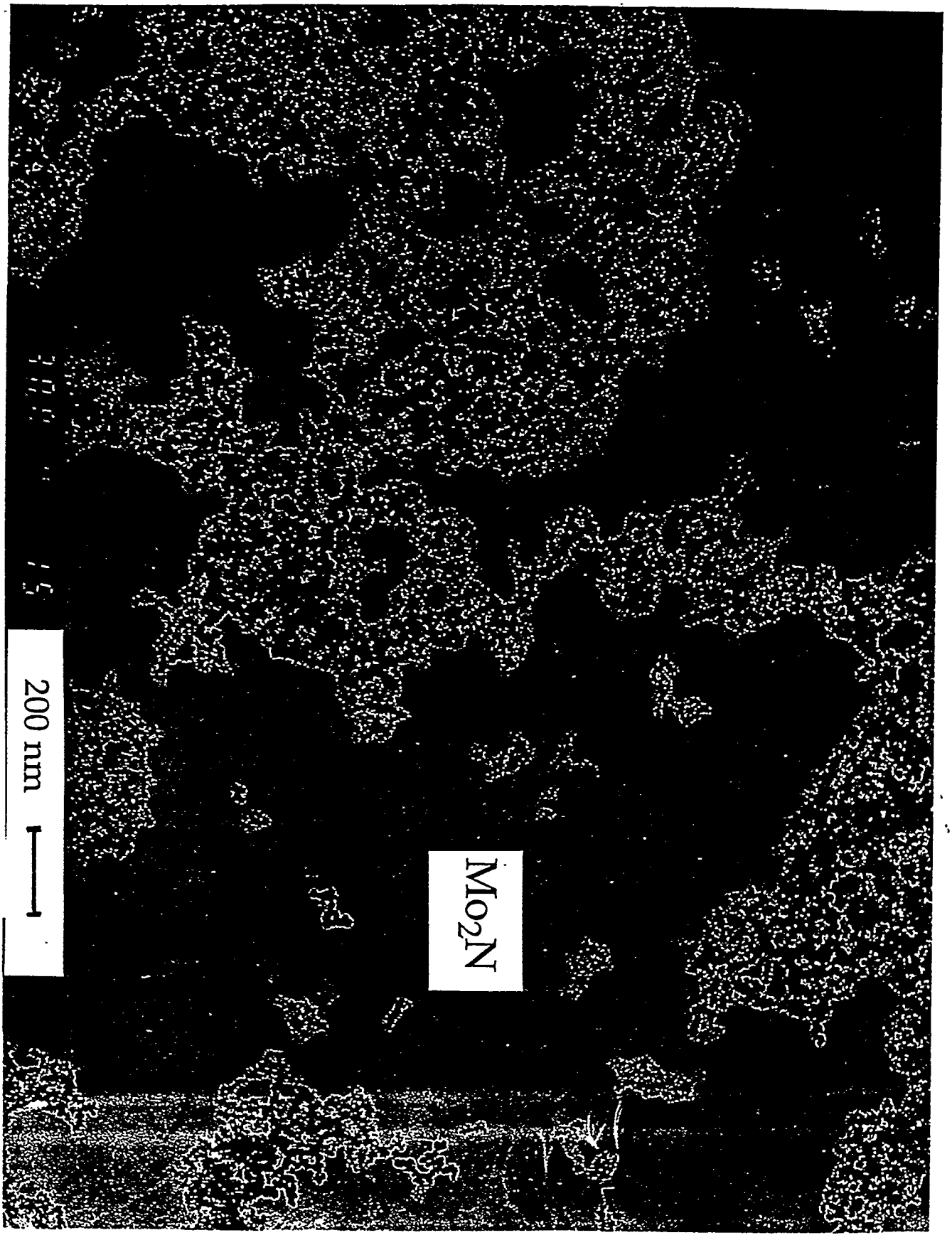


Fig. 8(c) TEM images of nanoscale Mo-nitride($Mo_2N$) particles.

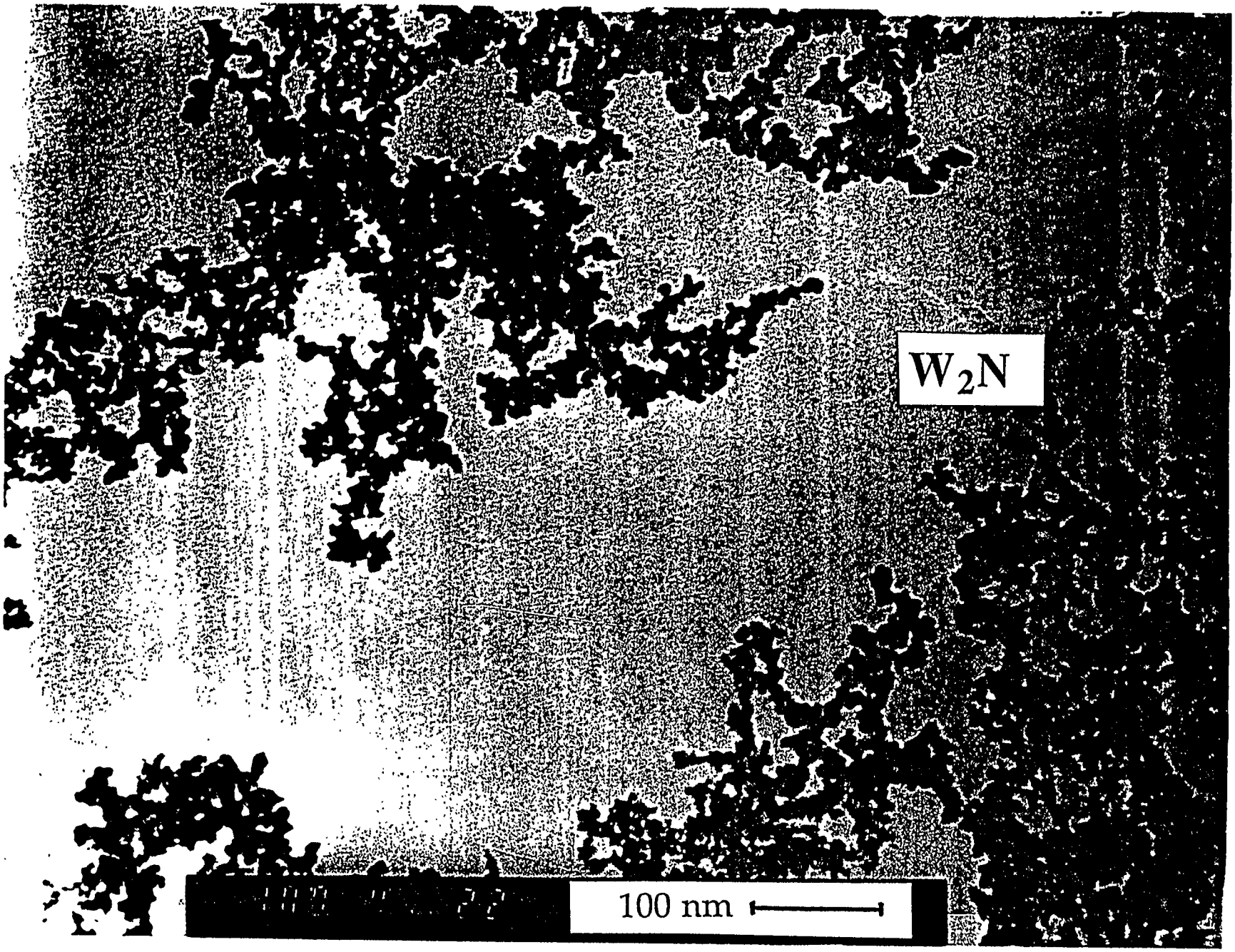


Fig. 8(d) TEM images of nanoscale W-nitride($W_2N$) particles.

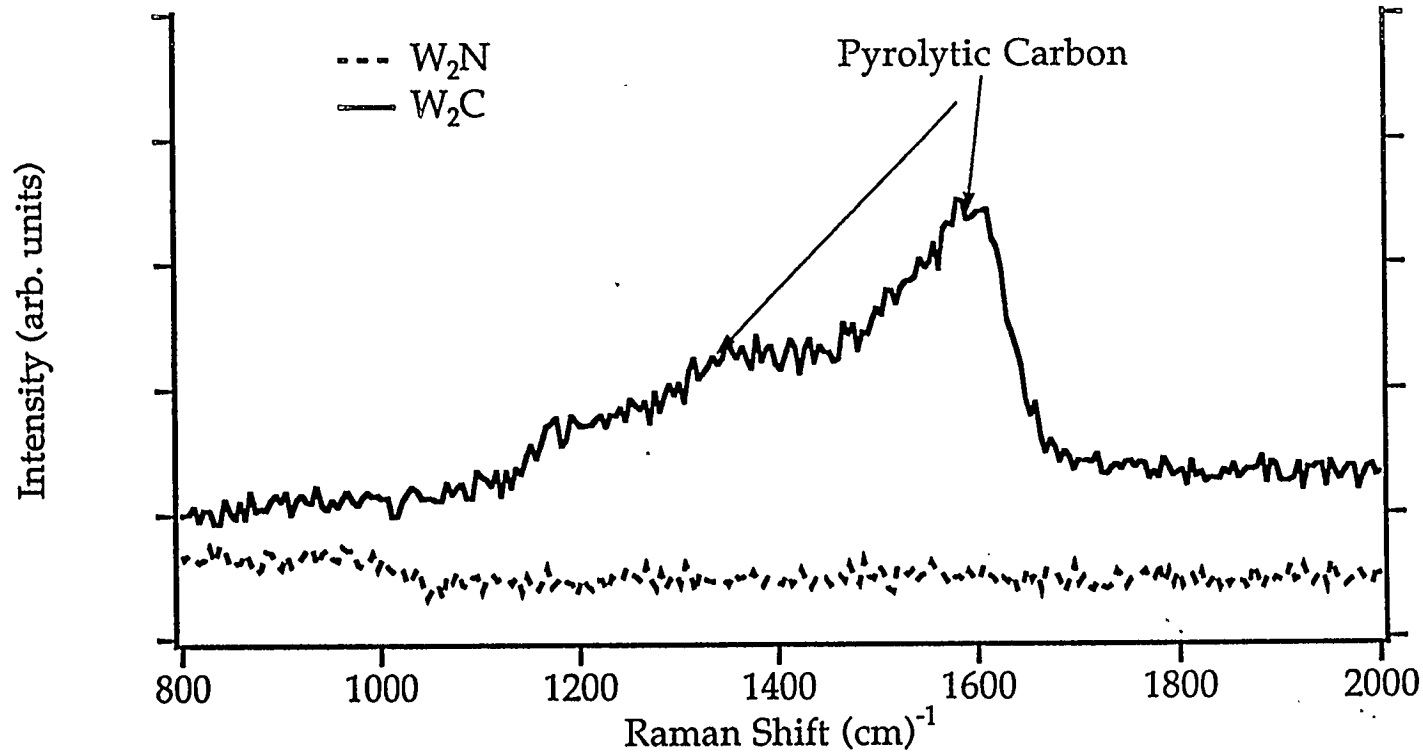


Fig. 9 Raman spectra($\lambda$=488 nm, Ar, T=300 K) of $W_2N$ and $W_2C$ particles. The peaks that are indicated by the arrows are associated with pyrolytic carbon coating on the particle surface.

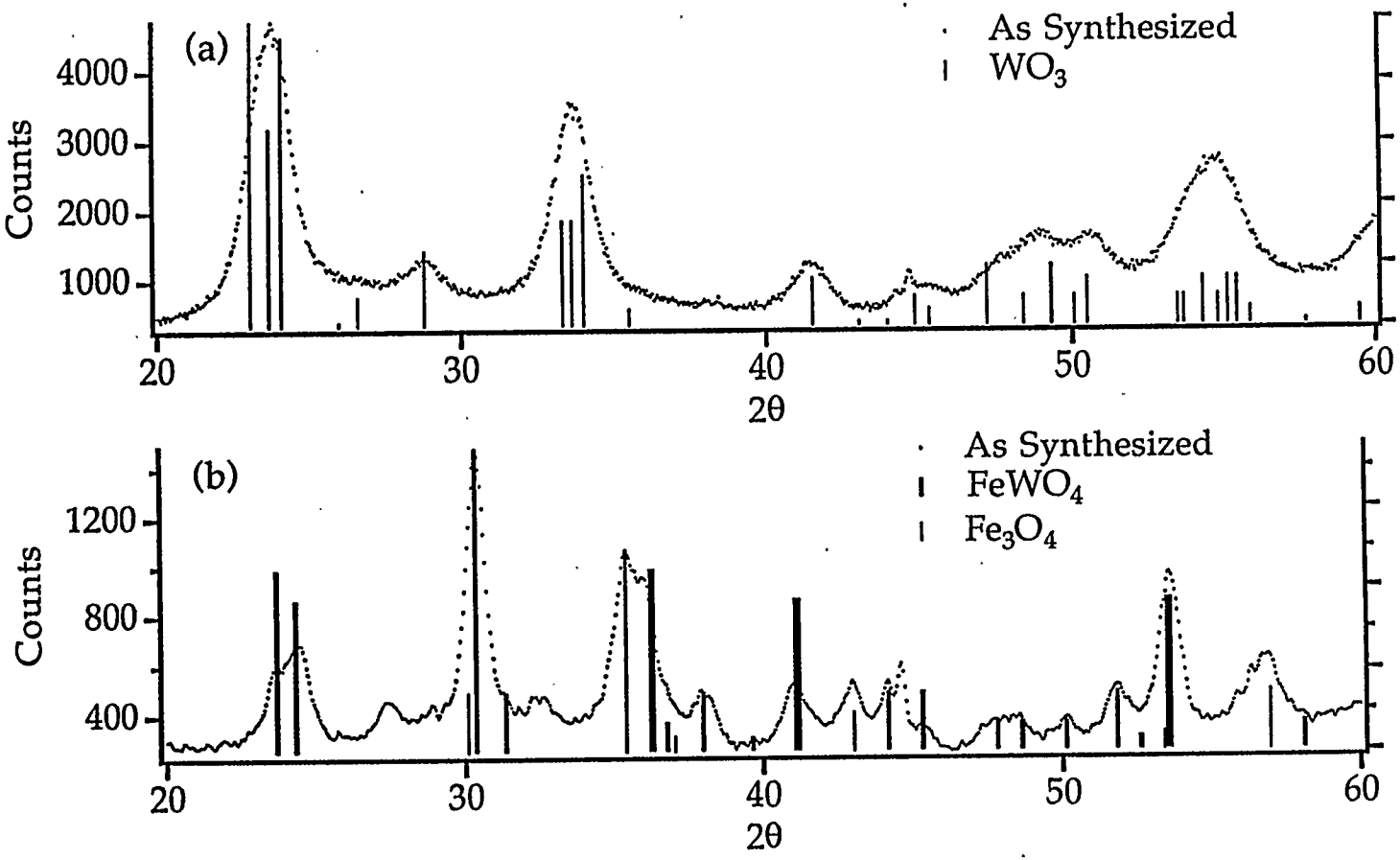


Fig. 10 (a) XRD data of W-oxide($WO_3$) nanoscale particles by pyrolyzing $W(CO)_6$ with $O_2$. (b) A mixture of nanoscale phases containing the ternary phase $FeWO_4$ as obtained by adding $W(CO)_6$ to the reaction zone. Vertical lines are from standard powder diffraction data files.

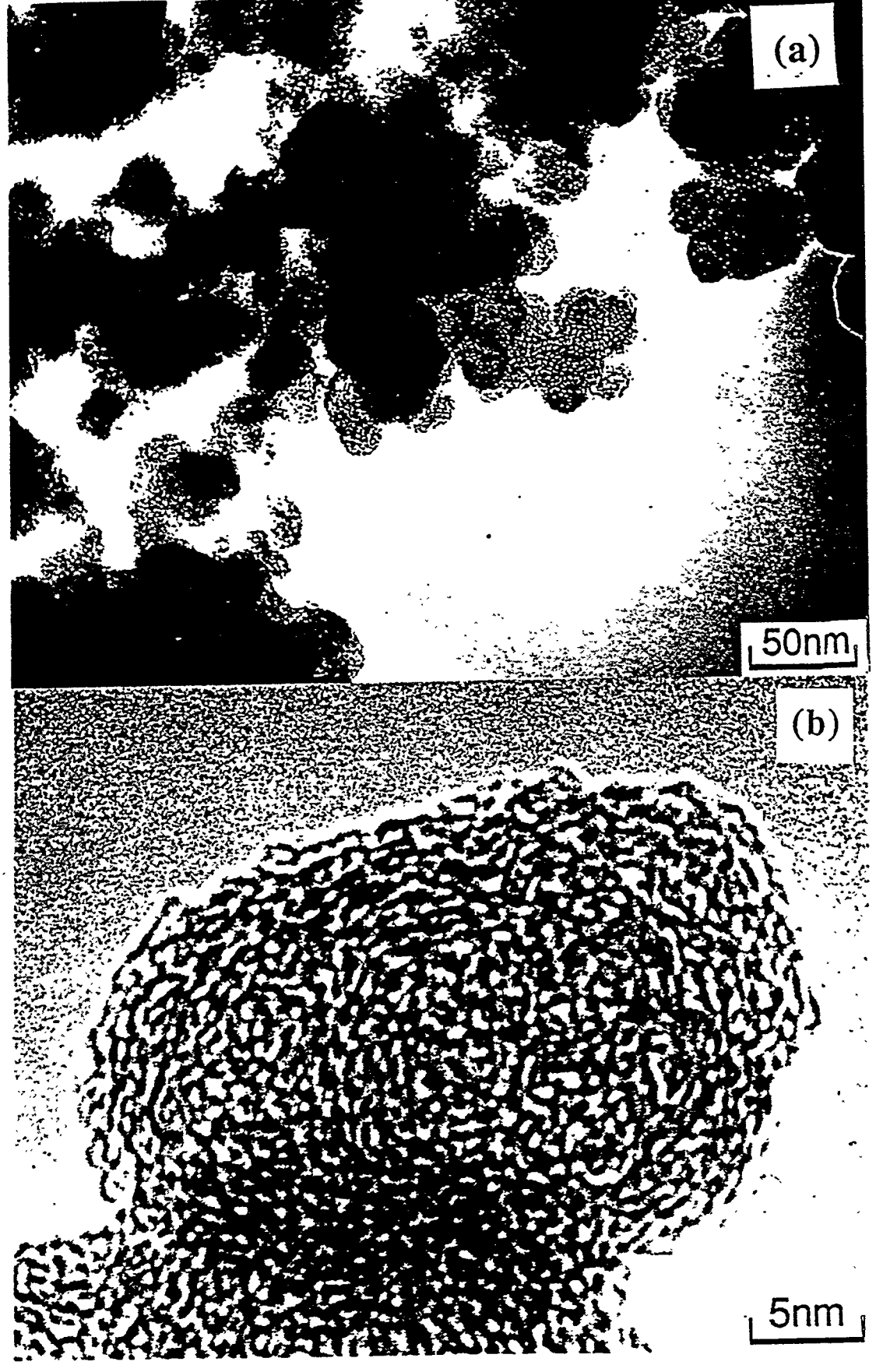


Fig. 11(a,b) High resolution TEM images for as synthesized carbon black particles from our laser pyrolysis system.

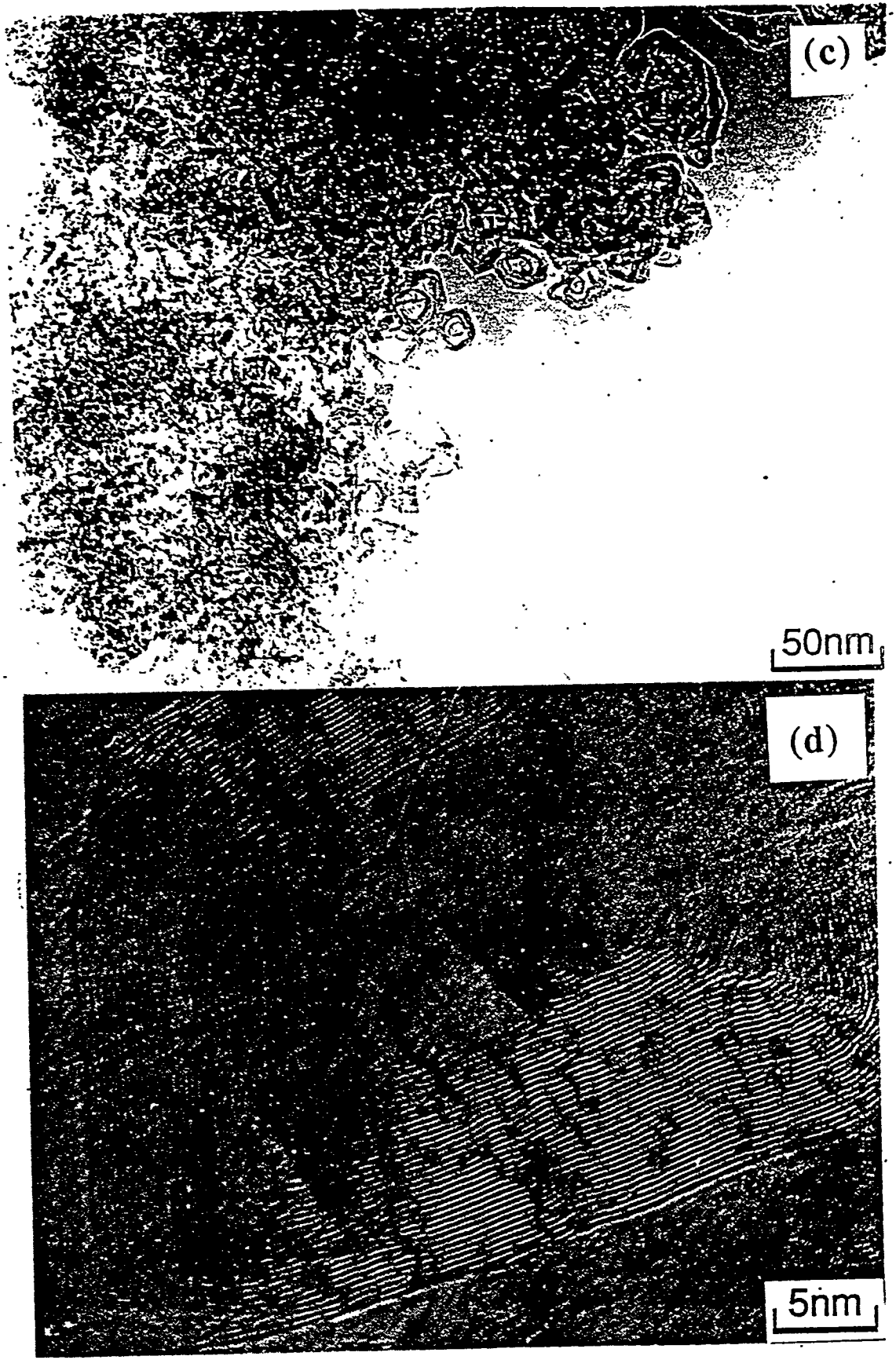


Fig. 11(c,d) High resolution TEM images for heat treated carbon black particles (2800 °C, in Ar)

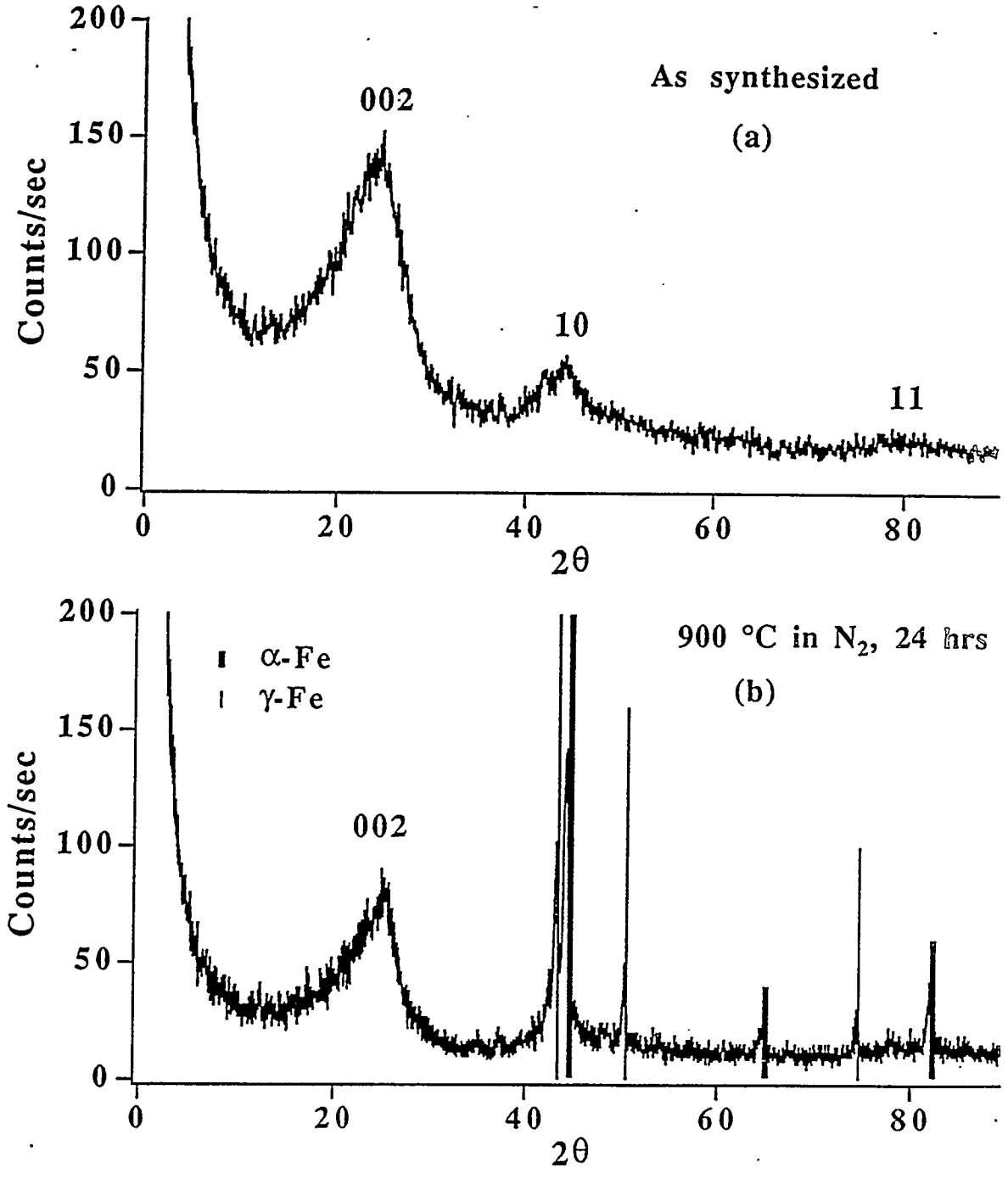


Fig. 12 XRD data for as synthesized carbon black particles (a) and heat treated particles (b) (900 °C, in $N_2$). Vertical lines represent standard powder diffraction data file for α-Fe and γ-Fe.

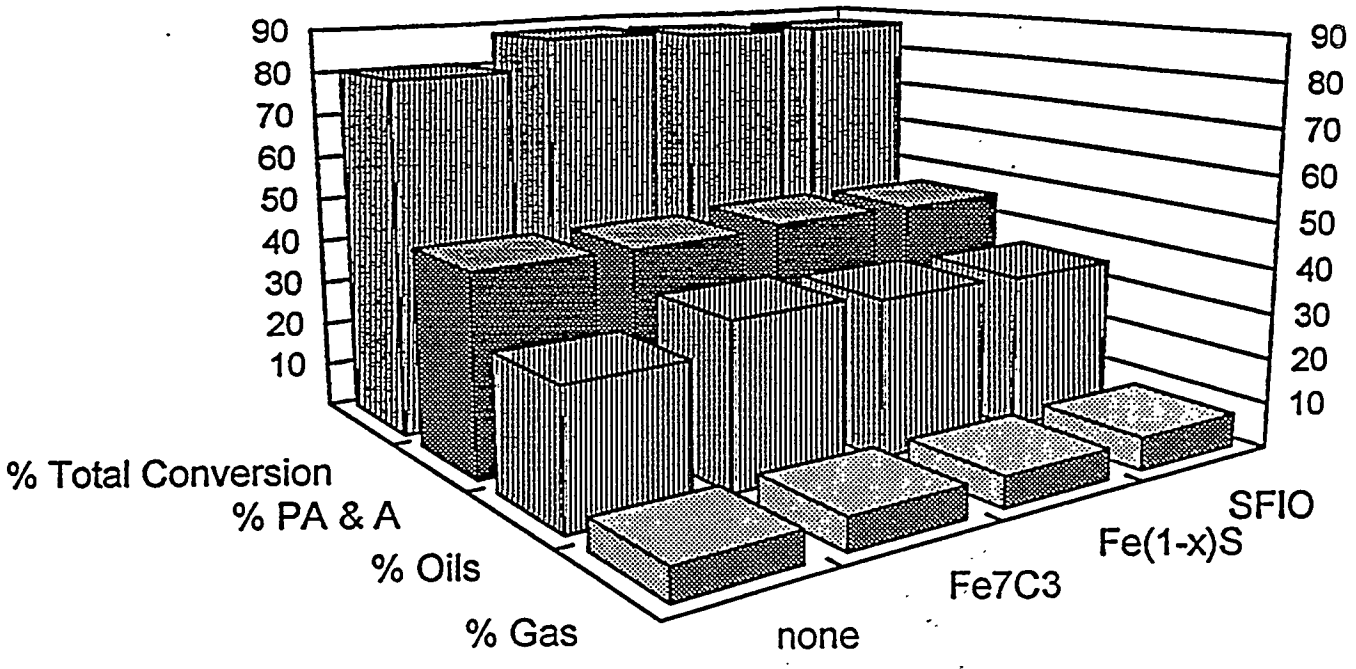


Figure 13 Effect of 0.7 wt% Fe Catalyst on Conversion at 415 C for 60 minutes

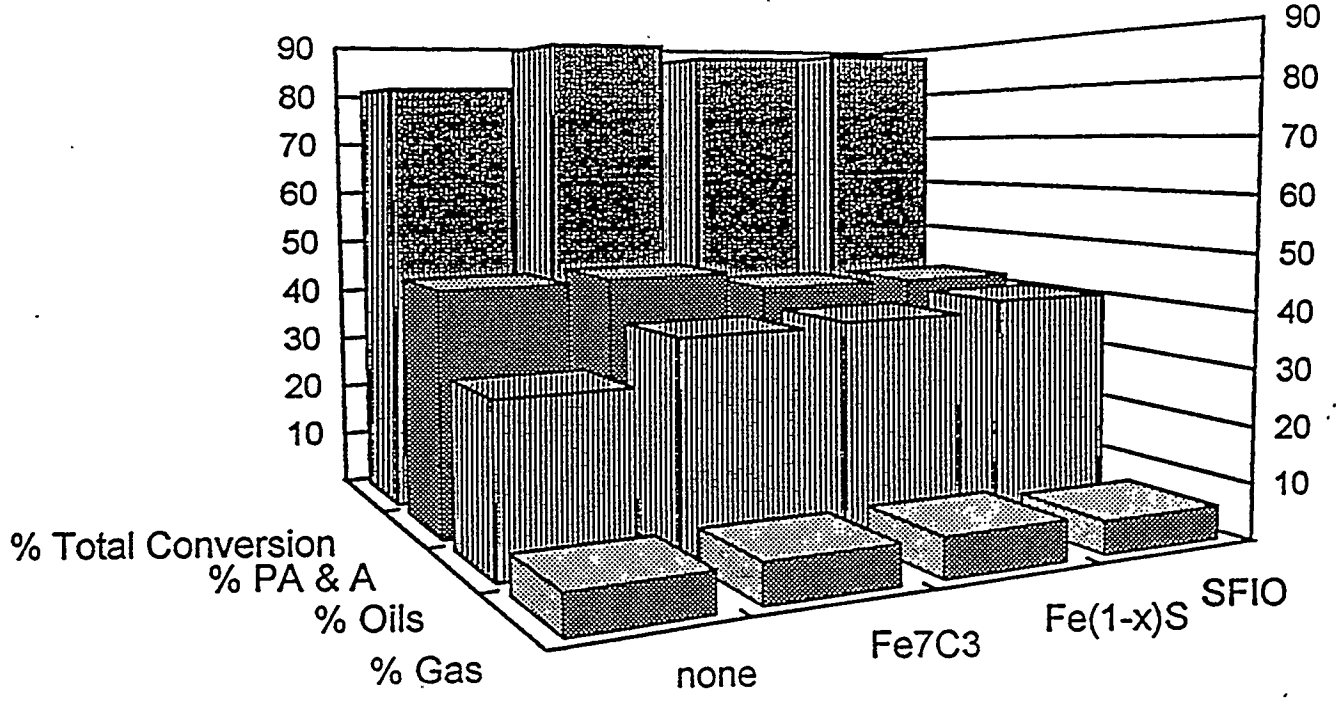


Figure 14 Effect of 1.4 wt% Fe Catalyst on Conversion at 415 C for 60 minutes

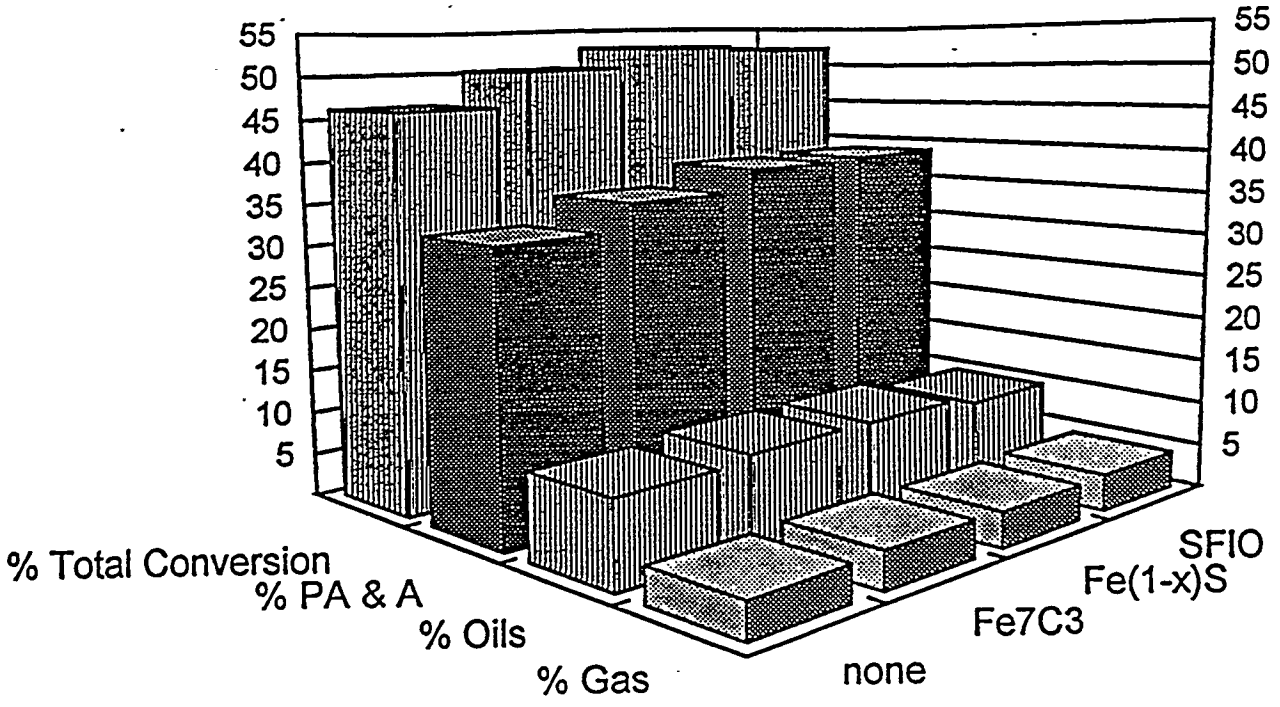


Figure 15 Effect of 0.7 wt % Fe Catalyst on Conversion at 385 C for 15 minutes

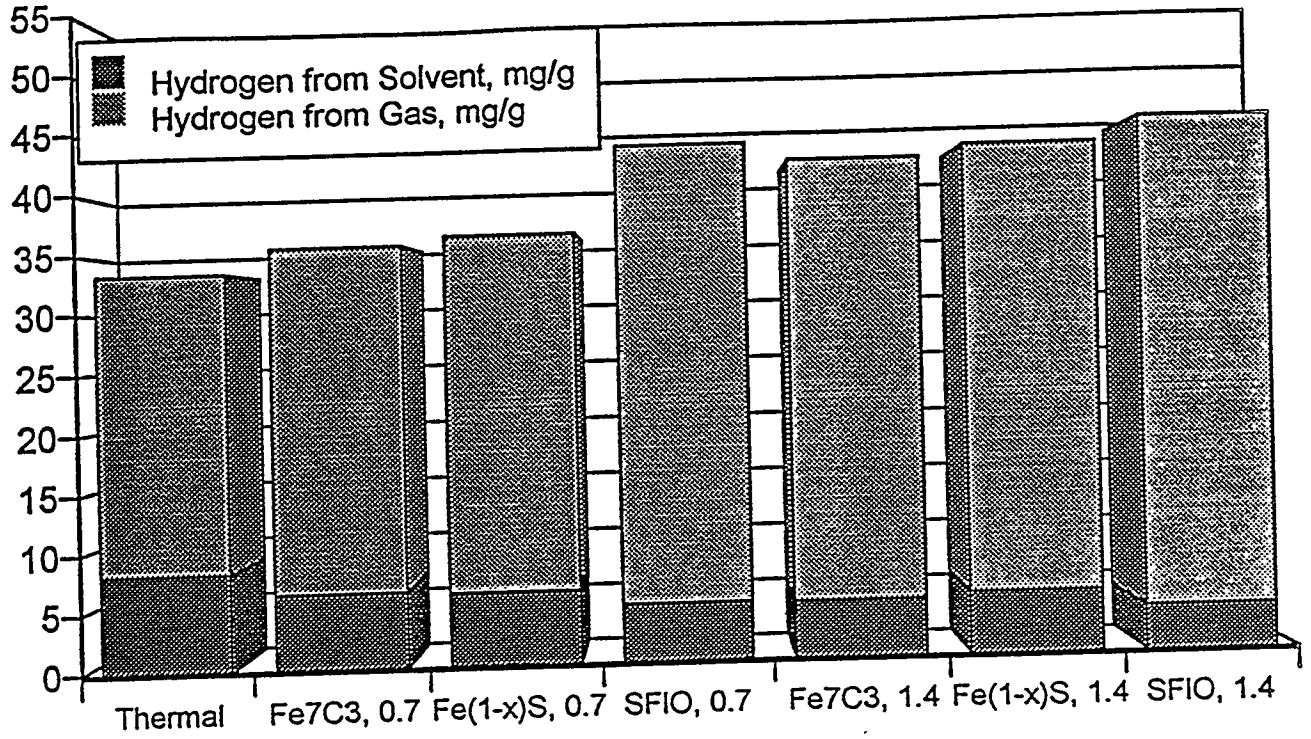


Figure 16 Effect of Catalyst on Hydrogen Consumption at High Severity

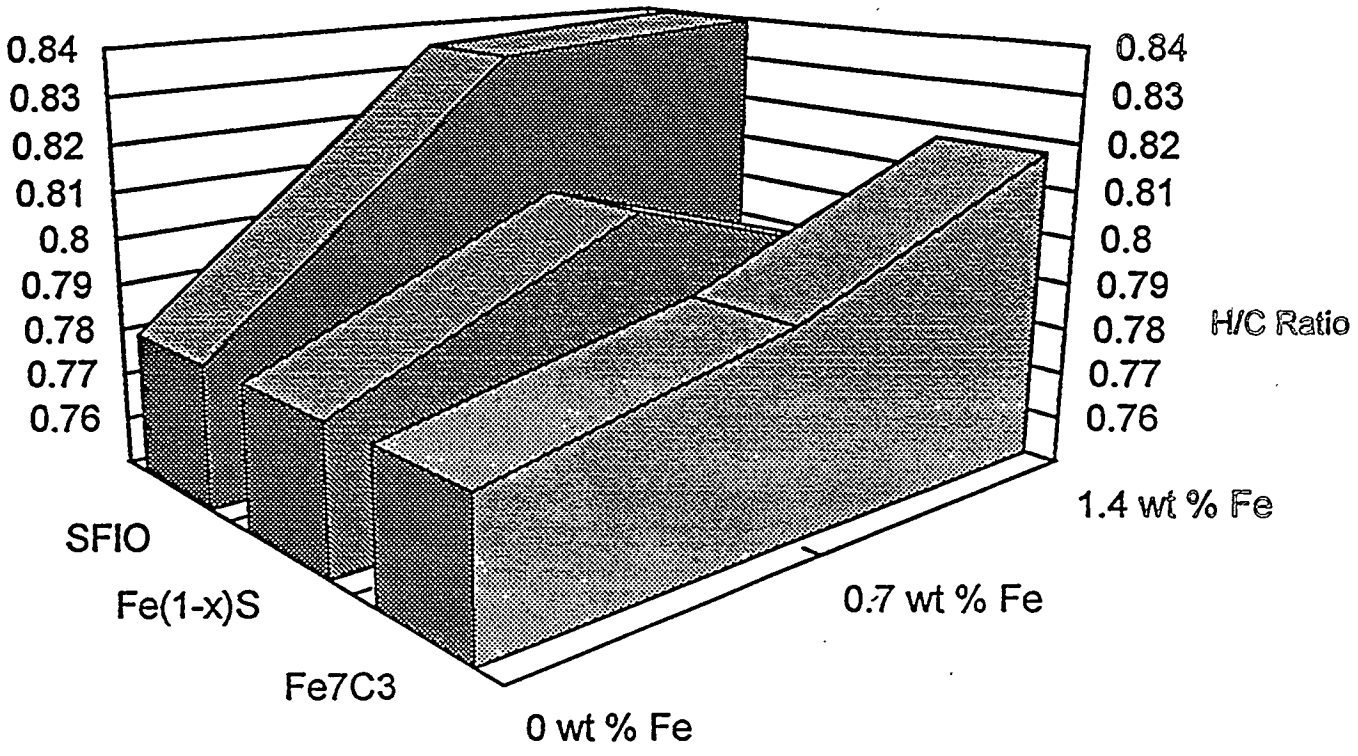


Figure 17 Effect of Catalyst Concentration on H/C ratio of PA&A fraction from high severity liquefaction experiments

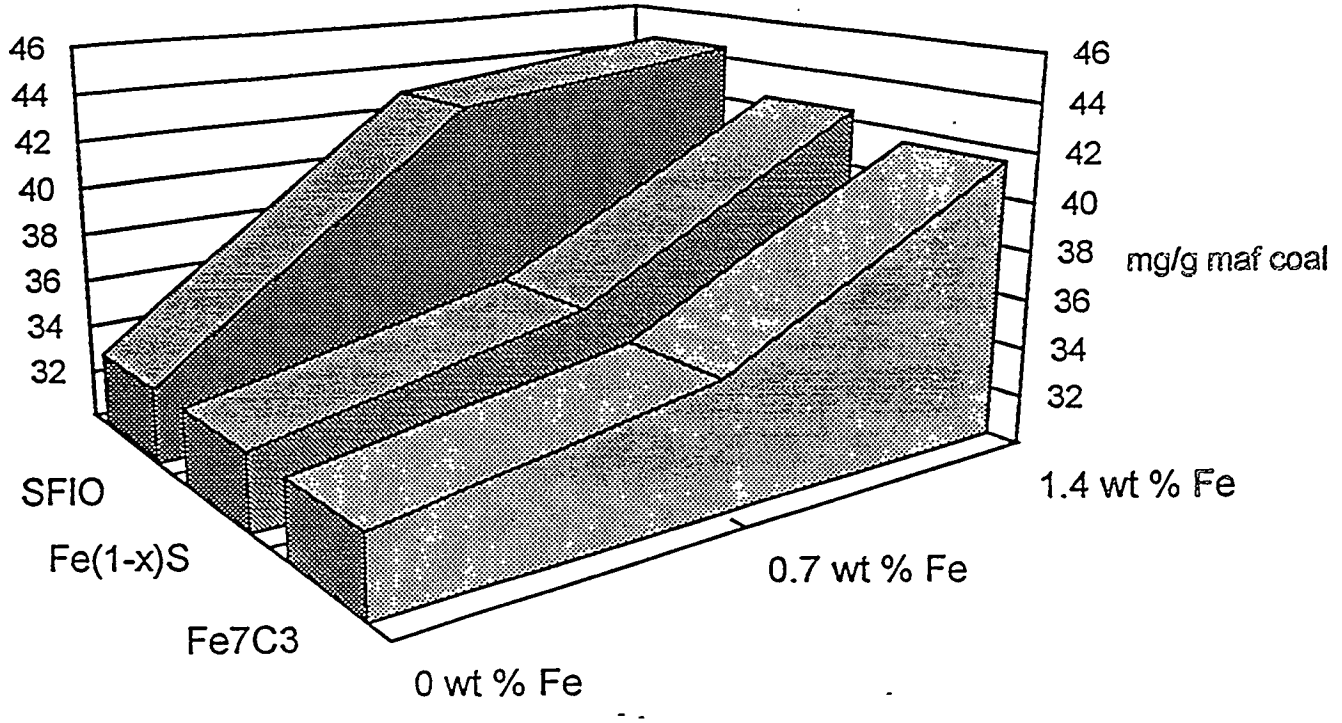


Figure 18 Hydrogen Consumption as a Function of Catalyst Concentration

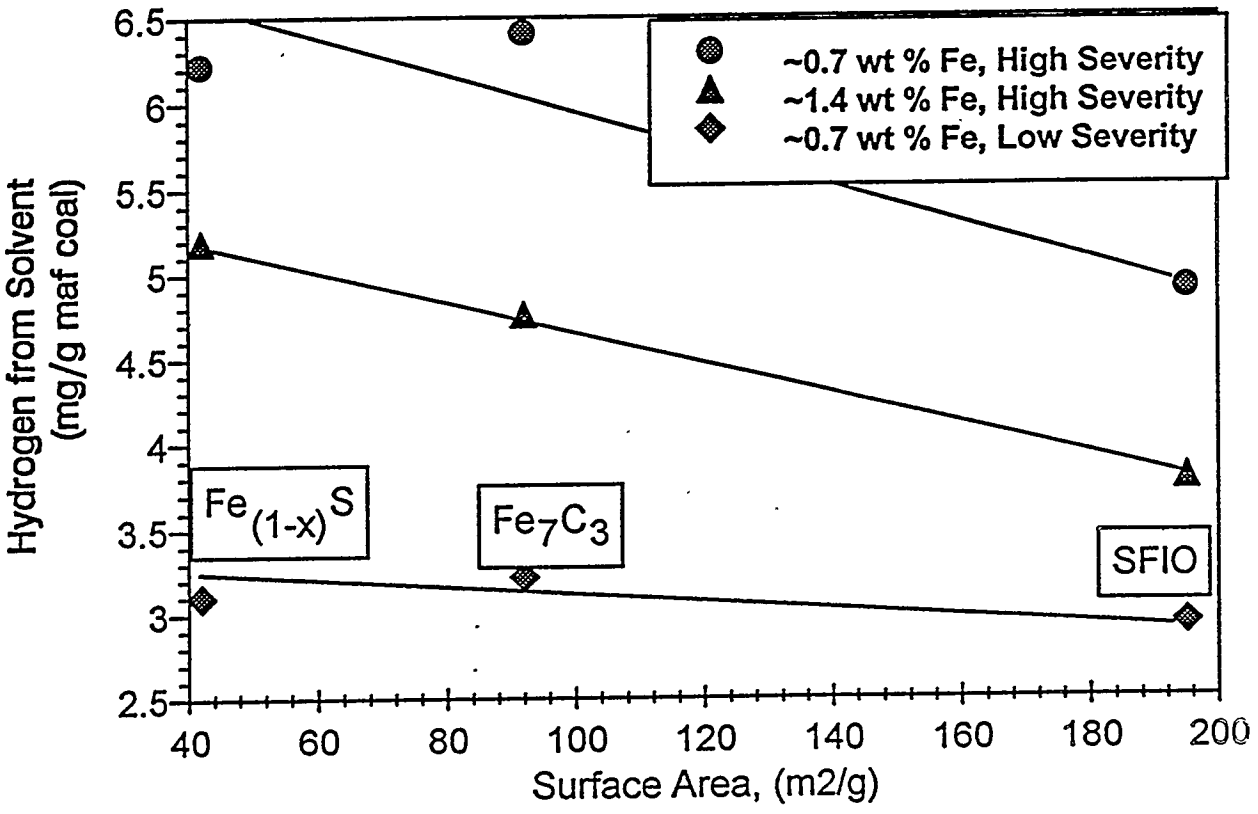


Figure 19 Effect of Surface Area on Solvent Dehydrogenation

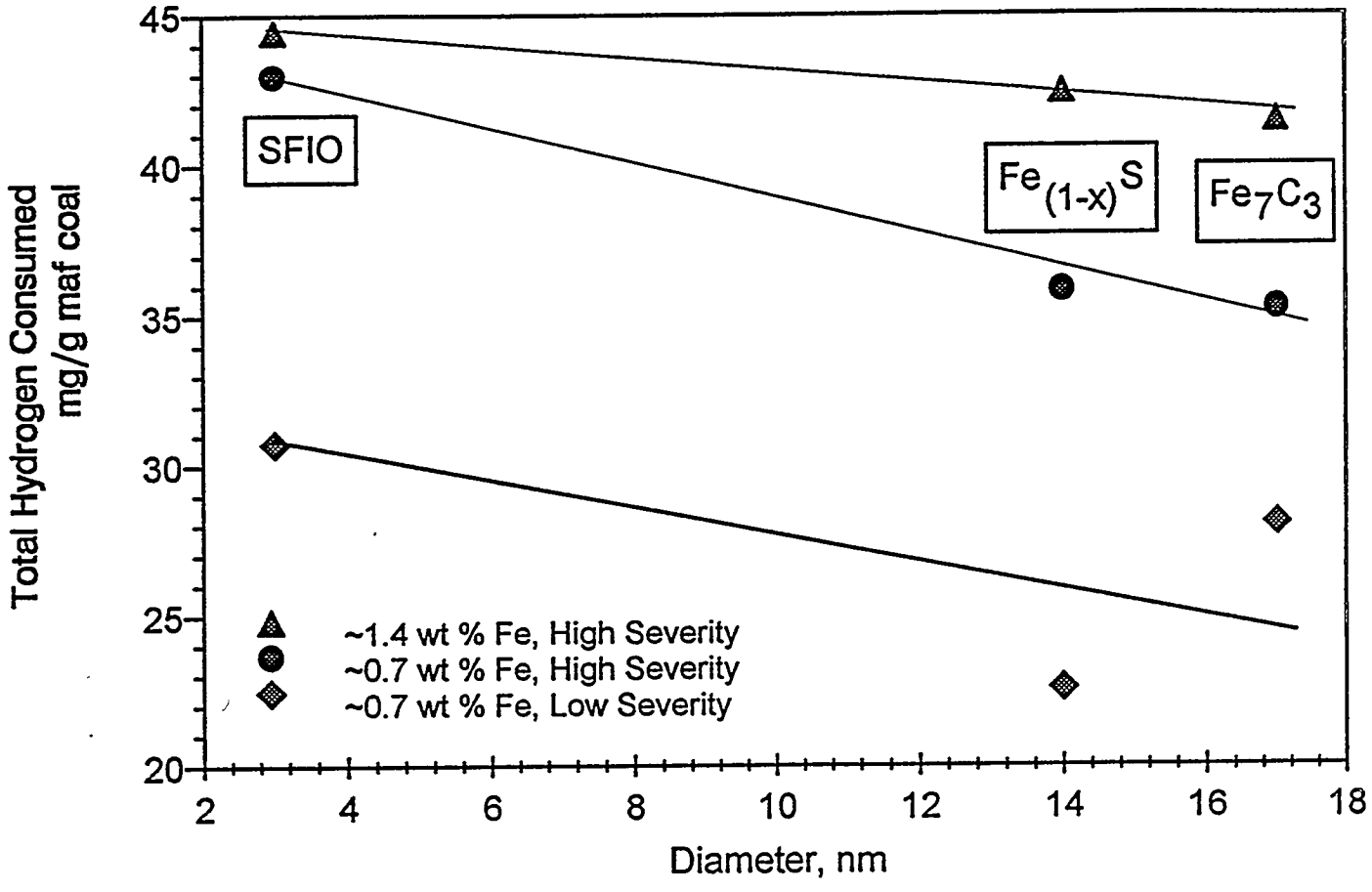


Figure 20 Effect of Particle Diameter on Total Hydrogen Consumption

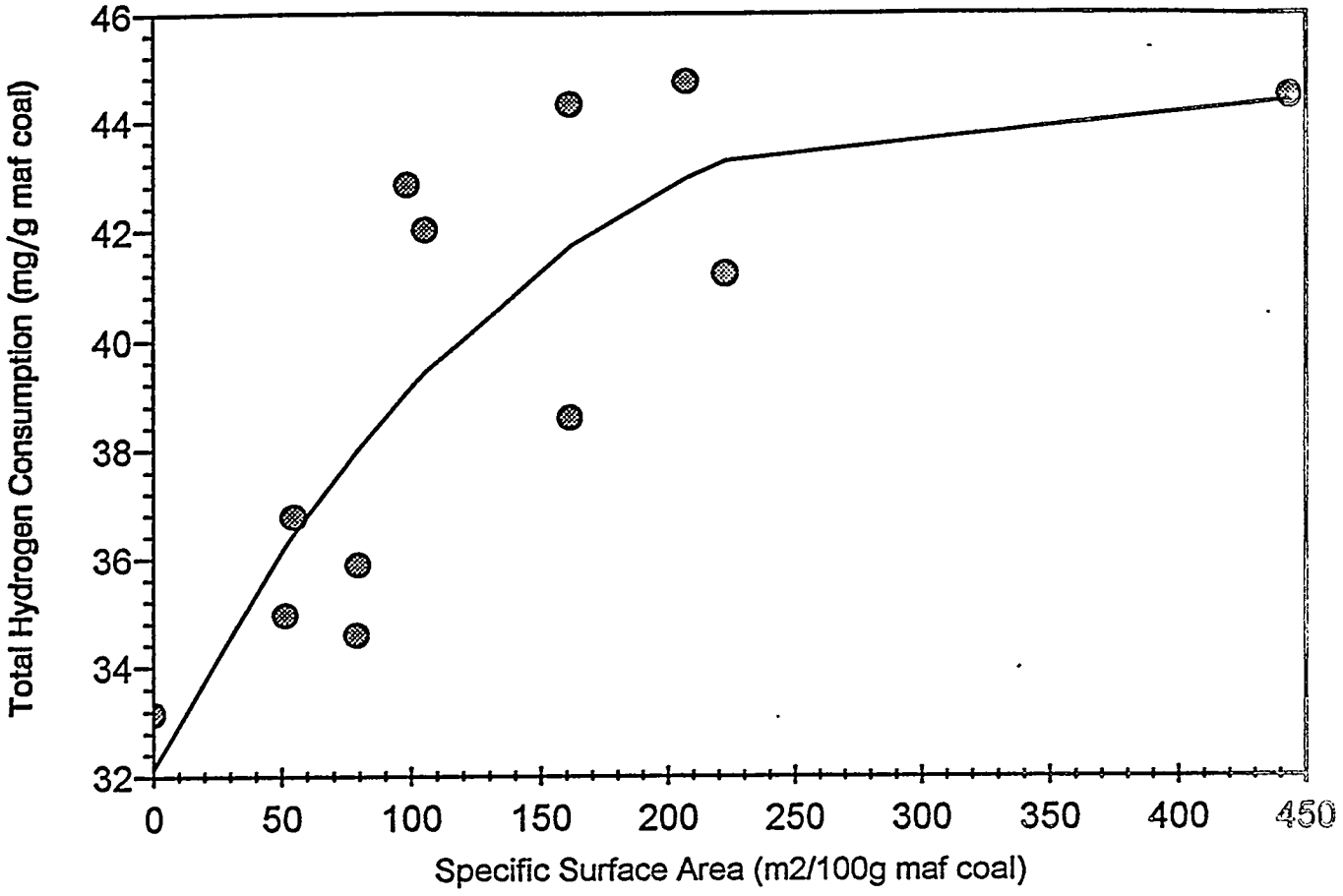


Figure 21 Effect of Specific Surface Area on Hydrogen Consumption